

Master of Science Thesis

Aeroacoustics of Cavity Flow using Time-Resolved Particle Image Velocimetry

D.Parkhi

November 1, 2009



Faculty of Aerospace Engineering



Delft University of Technology

Aeroacoustics of Cavity Flow using Time-Resolved Particle Image Velocimetry

Master of Science Thesis

For obtaining the degree of Master of Science in Aerospace Engineering
at Delft University of Technology

D.Parkhi

November 1, 2009



Delft University of Technology

Copyright © Aerospace Engineering, Delft University of Technology
All rights reserved.

DELFT UNIVERSITY OF TECHNOLOGY
DEPARTMENT OF AERODYNAMICS

The undersigned hereby certify that they have read and recommend to the Faculty of Aerospace Engineering for acceptance the thesis entitled "**Aeroacoustics of Cavity Flow using Time-Resolved Particle Image Velocimetry**" by **D.Parkhi** in fulfillment of the requirements for the degree of **Master of Science**.

Dated: November 1, 2009

Supervisors:

prof. dr. F. Scarano

dr. S.J. Hulshoff

dr.ir. B. W. van Oudheusden

ir. Valentina Koschatzky

Abstract

The flow past open cavities is a problem that is encountered in many engineering applications and can result in intense acoustic tones. The flow physics and acoustics of cavity configurations are complex and both computational and experimental techniques are being developed to provide an opportunity to gain further understanding and provide a tool to predict not only cavity tone frequencies but their amplitude.

In this thesis, noise produced due to low subsonic flow around a rectangular cavity has been studied by ‘visualising’ the flow around it. The flow visualisation was done by an experimental technique called Time-Resolved Particle Image Velocimetry (TR-PIV) which allowed us to measure velocity field around the cavity with high spatial and temporal resolution. The pressure fields were then obtained from the velocity fields by a technique called Planar Pressure Imaging(PPI). The sound emitted by the cavity flow was obtained from the pressure data by implementing Curle’s acoustic analogy. The pressure computed from PPI and acoustic pressure computed from the acoustic analogy were compared with the measurements from microphones located on the cavity surface and in the acoustic-field respectively.

The acoustic feedback was identified to be the dominant flow mechanism. The spectrum of acoustic pressure obtained from Curle’s Analogy and Microphone measurements showed presence of peaks corresponding to Rossiter mode 2 as well as harmonics of it. Although, there was an underestimation of sound pressure level, especially at the tonal peaks, Curle’s analogy was able to capture the location of these tonal peaks and trend in broadband frequencies. It is concluded that Particle Image Velocimetry has the potential to develop into a powerful tool for aeroacoustic measurements. It is recommended that better processing tool be developed to estimate the velocities and pressure near the walls which are affected by reflections. Further study of cavity flow should be done using Tomographic PIV to account for three dimensionality of cavity flow. Advanced digital signal processing algorithms must be used to study the acoustic data.

Acknowledgments

I wish to extend my sincere gratitude to Prof. Fulvio Scarano, for his enthusiastic supervision during my entire thesis. The opportunity to work with him was a great honour and challenge for me. He helped me to adapt to the process of scientific work and was sympathetic towards the difficulties I experienced during my thesis.

I would like to thank Valentina under whose guidance I participated in the experiments and Peter Moore for providing the pressure solver and spending time with me in evaluating the code. I owe my sincere thanks to Ferdinand, Roeland, Ragni and Arjen for their valuable comments and constructive criticism. Special thanks to Valerio with whom I spent invaluable time discussing aeroacoustics.

I take this opportunity to thank my dear friends, Nestor and Jabus who were always there for me during the stressful times as well as in celebrations. I wish to thank Prem and Siddharth for their guidance and support since I started my studies in Delft.

I cannot end without thanking my family, on whose constant encouragement and love I have relied throughout my time abroad. It is to them that I dedicate this thesis.

Table of Contents

Abstract	v
Acknowledgments	vii
List of Figures	xiii
1 Introduction	1
2 Cavity Flow Physics	5
2.1 Introduction	5
2.2 Driving mechanism	5
2.2.1 Fluid-dynamic mechanism: Acoustic feedback	5
2.2.2 Fluid-resonant mechanism	7
Passive cavities:	7
Active cavities:	7
2.2.3 Fluid-Elastic Mechanism	8
2.3 Leading parameters	8
2.3.1 Geometrical parameters	8
2D and 3D :	8
Shallow and Deep:	8
Open and Closed:	8
2.3.2 Flow parameters	8
Mach number:	8
Boundary layer thickness:	9
Reynolds number:	9
Shear-layer mode and wake mode:	9

3 Aeroacoustics	11
3.1 Introduction	11
3.2 Sound and its properties	11
3.3 Description of sound propagation using linear acoustics	12
3.4 Computational aeroacoustics	12
3.4.1 Direct approaches	13
3.4.2 Hybrid approaches	13
3.5 Experimental aeroacoustics	13
3.5.1 Particle Image Velocimetry and Acoustic Analogy	13
3.5.2 Microphones	13
3.6 Aeroacoustic analogies	14
3.7 Lighthill's analogy	14
3.8 Curle's analogy	15
3.9 Modified Curle's Equation with Simplifying Assumptions	16
3.9.1 Basic assumptions:	16
3.9.2 Spatial derivative to temporal derivative	17
3.9.3 Simplifying assumptions	17
3.9.4 Acoustic compactness	18
3.9.5 Efficiency of Sources	19
Sound from Volumetric Sources (V1, V2, V3) :	19
Sound from Surface Sources (S1, S2) :	20
3.9.6 Near field sound predictions	20
3.9.7 Far field sound prediction	21
3.9.8 Gutin's principle	22
3.10 Implementation of acoustic analogy to cavity flow	22
3.10.1 Analytical Formulations	22
3.10.2 Numerical Implementation	23
4 Particle Image Velocimetry	25
4.1 Parameters which influence PIV measurements :	27
4.1.1 Flow Seeding	27
4.1.2 Illumination	28
4.1.3 Light Sheet Formation Optics	28

Table of Contents	xi
--------------------------	-----------

4.1.4	Particle Image Formation Optics	29
4.1.5	Digital Image Recording	30
CCD sensor	30
CMOS sensors	31
f-stop and imaging:	31
Camera shuttering time	31
4.2	Digital PIV Evaluation	33
4.2.1	Frequency domain based correlation	34
4.3	Limitations of Digital PIV Evaluation	34
4.4	Advanced Digital Interrogation Techniques	35
4.4.1	Image normalisation	35
4.4.2	Window Off-Setting	35
4.4.3	Window Deformation	36
4.5	Window Deformation Iterative Multigrid Algorithm	36
Multi-Grid Analysis:	36
Iterative Analysis with Image Deformation:	36
4.6	Time Resolved-PIV	37
5	Planar pressure imaging	39
5.1	Introduction	39
5.2	Mathematical formulation	39
5.2.1	Acceleration	40
5.2.2	Viscous terms	40
5.2.3	Boundary conditions	40
5.3	Classification of PPI methods	40
5.3.1	Planar poisson formulation using Eulerian approach	41
5.3.2	Direct spatial integration using Eulerian approach	41
5.3.3	Direct spatial integration using Lagrangian approach	42
5.3.4	Planar poisson formulation with Lagrangian approach	42
5.4	Planar pressure imaging of cavity flow	43
6	Experimental Investigation	45
6.1	Experimental facility	45
6.2	Experimental Set-up	46
6.3	Data reduction techniques	47

7 Results and Discussions	49
7.1 Cavity Flow Physics	49
7.1.1 Time averaged flow features	49
7.1.2 Unsteady flow	50
7.1.3 Pressure fluctuations	53
7.2 Comparison of PPI results with microphone measurements	55
7.3 Aeroacoustics of cavity flow	58
7.3.1 Comparison of acoustic computations with microphone measurements . .	58
7.4 Sound generated at different Free Stream Velocities	60
8 Conclusion and Recommendation	63
8.1 Conclusions	63
8.2 Recommendation for future work	64
Bibliography	65
A Computational Aeroacoustics (CAA)	69
A.1 Direct Approaches	69
A.2 Hybrid Approaches	70
B Sonoion 8000 Microphones	73

List of Figures

1.1	Airframe noise is a significant component of overall noise	1
1.2	Cavity noise sources	2
2.1	Schematic Representation of Cavity-flow	6
2.2	Schematic of deep (a) & shallow cavities: open (b), transitional (c), closed (d) (reproduced from Gloerfelt)	9
3.1	Lighthill's Analogy for a Turbulent Jet	15
3.2	Schematic of source and sound scales	19
3.3	Implementation of acoustic analogy from data generated from PIV-PPI	23
4.1	Schematic of a typical PIV measurement system	25
4.2	Scattering directivity of tracer particles	28
4.3	Schematic of PIV optics	29
4.4	Normalized intensity distribution of the Airy pattern and its approximation by a Gaussian bell curve.	30
4.5	Digital imaging of small particles	31
4.6	Timing diagram based on Double Frame/Single Exposure frame straddling mode	32
4.7	Block diagram of the Digital PIV Evaluation	33
4.8	Normalisation of raw images before cross-correlation	35
4.9	Window Off-Setting and Window Deformation	35
4.10	Window Deformation in Iteration Loop	36
5.1	Schematic of pressure integration paths by Baur and Kongeter	42
5.2	Domain and Boundaries for pressure computation using PPI	43
6.1	Experimental Facility	45
6.2	Experimental Set up	46

7.1	Mean quantities in the flow at $U_e = 10\text{m/s}$, laminar incoming boundary layer	50
7.2	Instantaneous velocity fields : streamwise(left) and vertical(right) in a shedding period for mean flow =10m/s	51
7.3	Time history and Power Spectrum of velocities near the trailing edge of cavity: $X = 0.9L$, $Y = 0$ at $U_e = 10\text{m/s}$	52
7.4	Velocity and Pressure at $y/D = 0$; $x/L = 0.95$ for $U_e = 10 \text{ m/s}$	53
7.5	Instantaneous Vorticity fields(left) and Pressure fields(right) in a shedding period	54
7.6	RMS of pressure measured by microphones and pressure computed by PIV-PPI at the same locations for mean flow $U_e = 10, 12 \text{ m/s}$	55
7.7	Comparison of PPI and microphone back wall at $U_e = 12 \text{ m/s}$	56
7.8	Comparison of PPI and microphone on the bottom wall at $U_e = 12 \text{ m/s}$	57
7.9	Comparison of OASPL of sound measured by microphone in acoustic with Curle's Analogy and Gutin's Principle	58
7.10	Comparison of sound measured by microphones with Curle's Analogy and Gutin's Principle at $U_e = 12 \text{ m/s}$	59
7.11	Variation of sound at M13 with in acoustic-field free stream velocity	60
7.12	Variation of sound with free stream velocity at M14 in acoustic-field	61
B.1	Schematic description of condensor microphones	73
B.2	Typical response curve for Sonion 8000 series microphones	74

Chapter 1

Introduction

Flow-generated sound is a serious problem in many engineering applications. It can cause severe discomfort to humans and affect stealth operations by military vehicles, MAVs and submarines. The aerodynamic noise of airplanes at take-off and in the approach configuration continues to be a critical factor in the future development of aviation. The most notorious of these noise sources is the flow noise from the aircraft jet-engines which continues to be an intense area of research. In fact, the study of aeroacoustics, pioneered by Lighthill (1952), was prompted by the need for quieter jet engines.



Figure 1.1: Airframe noise is a significant component of overall noise

With advances in jet-noise reduction, fan noise from the turbo-fan engines rises in significance. Airframe noise has also become a significant component of overall noise, especially when landing. Noise from the landing gear, slats, and flaps etc. are categorized under airframe noise. It can be seen from the Figure (1.1) airframe noise has its highest levels on the

approach to landing with the full high-lift devices operational and the undercarriage down with engines at approach settings. The typical Mach number varies between $M = 0.2$ and 0.3 .

Aviation technology with dramatically lower community noise footprint, for example one that limits the noise footprint to the airport perimeter, is envisioned in FLOVIST(Flow Visualization Inspired Aero-acoustics by Time-Resolved Tomographic Particle Image Velocimetry) a 5-year project sponsored by the European Research Council (ERC). The project aims at developing and demonstrating an innovative experimental approach to investigate the sound produced by airflows around aircrafts. This research programme contributes towards the European mission to develop greener airplanes for a sustainable air transport.

Cavity noise is one of the most important airframe noises. During landing, they occur from open wheel wells after the undercarriage has been lowered. For the military aircrafts, the weapon bays experience flow-induced oscillations which can even excite the vibrational modes of the aircraft structure. For ground transportation at low Mach number, the automobile industry is concerned with the noises produced by the door gaps, the side mirror and the open sun-roof and how they affect the comfort in the car.



Figure 1.2: Cavity noise sources

As a first step towards understanding the sound generation mechanisms of these cavities: the wheel wells, weapon bays and door gaps can be modeled as rectangular cavities and the

unperturbed flow outside the cavity regarded as effectively uniform. Even such a simple geometry (with uniform external flow) is rich in diverse dynamic and acoustic phenomena which is complicated by a possible aeroacoustic feedback loop or resonance depending on the shape, size of cavity and flow conditions. When flow passes over a cavity or opening, due to vortex shedding at the upstream edge of the cavity, intensive tone noises may be generated. Aerodynamicists, for over half a century, have made attempts to explain the flow mechanism in a rectangular cavity through various techniques : numerical and experimental, with varying degrees of success. However, accurate simulation and measurement of flow over a rectangular cavity is only half the challenge. The greater challenge is to predict the sound generation mechanism from the cavity flow.

In 1952 Lighthill formulated for the first time the science of how sound is created. By simply rearranging the Navier-Stokes equation, he was able to derive an ‘Acoustic Analogy’ to predict noise produced by a turbulent fluid motion in an ambient or stationary environment. If a complete description of fluid motion is known acoustic analogy can be applied to calculate sound produced by it. Various numerical schemes are being employed in computational fluid mechanics to describe cavity flow dynamics accurately. However, the numerical techniques suffer from various drawbacks such as long computational time, excessive memory requirements and numerical errors.

The FLOVIST project proposes an innovative experimental approach to ‘visualise’ a turbulent flow by seeding the flow with small particles which faithfully follow the flow and recording their images with high speed cameras. By tracking these particles in consecutive images it is possible to recreate the flow on computers and quantify them with high accuracy. An appropriate acoustic analogy is then applied to compute noise radiated by the flow.

Goal of the thesis project

The goal of this thesis project is to predict the sound produced by laminar flow over a rectangular cavity by measuring two dimensional flow fields using a technique called Temporally-Resolved Particle Image Velocimetry. This powerful technique will be used to measure the two dimensional velocity vectors in the flow with very high temporal and spatial resolution. The velocity data will then be fed into a planar pressure solver to obtain pressure fields in the cavity flow. An Acoustic Analogy, originally proposed by [Lighthill \(1952\)](#), and modified by [Curle \(1955\)](#) will then applied by the author to the pressure field data to compute sound pressure level in acoustic-field . Microphone measurements at cavity walls and in far-field will also be made to validate the pressure and acoustic computations.

Chapter 2

Cavity Flow Physics

2.1 Introduction

The phenomenon of flow-induced noise radiation and acoustic oscillations in a rectangular cavity has been studied by numerous investigations in the past. While the geometric configuration is rather simple, many experimental observations have shown a flow phenomenon rich in unsteady fluid dynamics, flow-acoustic interaction, and flow-acoustic resonance. This complex flow is often accompanied by an intense acoustic radiation that produces both discrete and broadband noise. The emphasis of earlier experimental investigations was mainly on the classification of cavity flow regimes and characterization of the generation of self-sustained oscillations in order to develop methods of active control. This is not an easy task as the noise generation mechanisms are dependent on many flow and geometric parameters, such as incoming boundary layer thickness, free stream Mach number, and length-to-depth ratio. The figure below shows the schematic of cavity flow and the parameters influencing its flow. In this chapter, an attempt has been made by the author to describe the driving mechanism of cavity flow and the parameters which effect them based on previous investigations.

2.2 Driving mechanism

The primary characteristic of cavity flows is self-sustained oscillations present both in the flow and acoustic field. It is typical of all cases where a shear layer dynamics are modified when a bluff body is introduced leading to enhanced organisation and self-sustained oscillations. The mechanism which drives the cavity flow was classified by [Rockwell and Naudascher \(1978\)](#) into three categories.

2.2.1 Fluid-dynamic mechanism: Acoustic feedback

[Rossiter \(1964\)](#) seemed to be one of the early investigators who suggested that the observed phenomenon was a result of acoustic feedback. His shadowgraphic observations indicated that concentrated vortices were shed periodically in the vicinity of the upstream lip of the cavity. These vortices traveled downstream along the shear layer which spanned the open end of the cavity. On the basis of this and other observations, Rossiter proposed the following model which he believed was responsible for generating the cavity tones. A vortex is shed

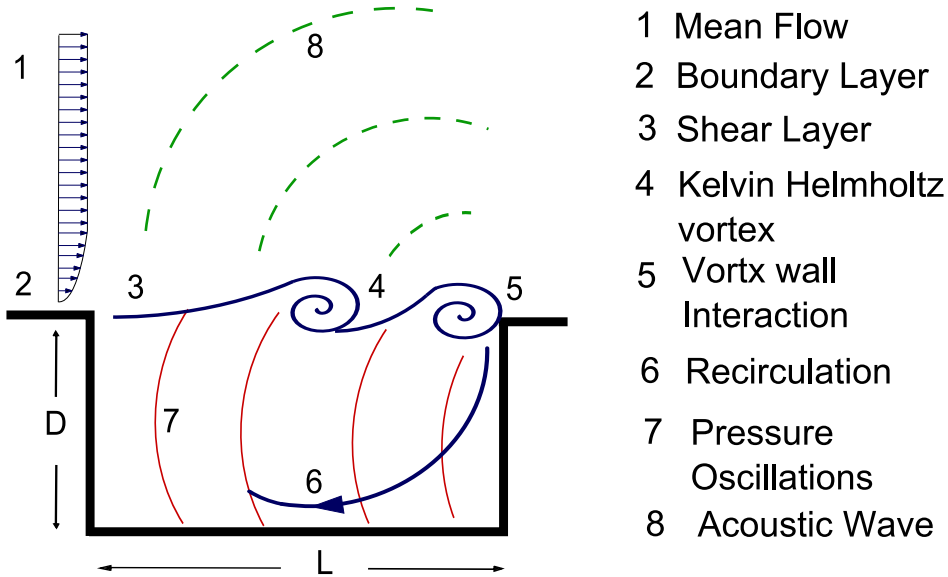


Figure 2.1: Schematic Representation of Cavity-flow

from the cavity leading edge and is convected downstream until it impinges onto the forward facing step, causing an acoustic wave, which travels upstream and leads to instabilities in the shear layer and to the shedding of a new vortex. Using the fact that the timing of the various links of the feedback loop must be synchronized, Rossiter derived the following semi-empirical formula for the tone frequencies:

$$\frac{fL}{U_e} = \frac{m - \gamma}{M + \frac{1}{k}} \quad (2.1)$$

where,
 f = frequency of tones,
 U_e = free-stream velocity,
 L = length of cavity,
 m = integer,
 M = Mach number,
 k = ratio of convection velocity of vortices to free-stream velocity,
 γ = spacing between the vortices.

Limitations of Rossiter's model :

1. The model does not provide numerical values for k and γ . They are treated as empirical constants to be determined by a best fit to measured data. Rossiter found that by taking $\gamma = 0.25$ and $1/k = 1.75$, the above equation agreed with his measured data very well.
2. Rossiter model does not describe how acoustic disturbances are generated at the downstream wall of the cavity or how the feedback acoustic waves excite the shear layer at the upstream lip.

In Rossiter model good deal of importance is attached to highly localized vortices, However, neither schlieren pictures taken by Krishnamurty nor water table visualization by Heler and Bliss indicated presence of these vortices during cavity oscillations in subsonic or supersonic regime.

Heller et al. (1971) used a correction factor in Rossiter equation to account for higher sound speeds in the cavity. This equation, referred to as modified Rossiter's equation, is given by

$$\frac{fL}{U} = N_{fm} = \frac{m - \alpha}{\frac{1}{k} + \sqrt{\frac{M}{1 + \frac{(\gamma-1)*M^2}{2}}}} \quad (2.2)$$

where, the empirical constant k is the ratio of the average instability wave convection velocity to free stream velocity and is a function of free stream Mach numbers greater than 0.4. According to Block (1976) the choice of $k = 0.57$ has proven to be in good, while Ahuja and Mendoza (1995) found this value closer to 0.65.

2.2.2 Fluid-resonant mechanism

The cavity enclosure in the vicinity of the shear layer can act as an acoustic resonator and may impose its preferred frequency and consequently alter flow dynamics. At low mach numbers, the resonant mechanism of the cavity can dominate the aeroacoustic feedback mechanism.

Passive cavities: Plumbelle claimed that the cavity are passive resonators which amplify select frequency of the broadband noise source present in the turbulent shear layer above it (*turbulent rumble*). Unfortunately, as pointed out by Rossiter (1964) this line of reasoning meets obvious difficulties when the (boundary layer) flow is laminar. Experimentally it is found that laminar-flow produces louder tones even though there is a complete absence of broadband excitation.

Active cavities: In this case, the shear layer instabilities provide the energy for the coupling with the feedback mechanism. The cavity closed by the shear layer can respond according to box modes, which are standing waves in longitudinal(L), crossflow(D) and spanwise(W) directions. An analytical derivation of acoustic modes of acoustic modes of two dimensional deep rectangular cavity for low-speed inviscid flows was realised by Tam (1976). He solved a wave equation by using the boundary condition imposed by cavity walls and radiation condition.

$$\omega_{m,n} = \pi \left[(n - 1/2)^2 / (D/L)^2 + (m - l)^2 \right]^{1/2}, m, n = 1, 2, 3, \dots \quad (2.3)$$

The depth-mode and Helmholtz resonances are the most common, but spanwise mode are, for instance observed for the door gaps.

2.2.3 Fluid-Elastic Mechanism

The third category of fluid-elastic phenomena considers the coupling of the flow with the structural modes of the cavity. The elastic displacement of a wall is the energy source. This mechanism is out of the scope of this project and will not be discussed henceforth in the report.

2.3 Leading parameters

The cavity flow dynamics and resulting noise generation mechanisms are dependent on many flow and geometric parameters. It is not an easy task to classify such wide variety of configurations. This section presents the attempts by [Ahuja and Mendoza \(1995\)](#) and Gloerfelt to enumerate parameters which effect the cavity flow.

2.3.1 Geometrical parameters

2D and 3D : Cavity flows are unsteady and highly three-dimensional (3D), even for a cavity of low length-to-width ratio (L/W), as observed by [Maull and East \(1963\)](#). With the use of a thin oil film it was demonstrated that across the width of a cavity, the spanwise line of separation at the bottom of the cavity was not straight, but exhibited an asymmetric wave-like pattern. As the L/D ratio increases, i.e. from a deep to a shallow cavity configuration, there is a sudden change in the pressure distribution corresponding to the collapse of the large vortical structures found in deeper cavities. While the flow field inside the cavity is highly three-dimensional (3D) ([Maull and East \(1963\)](#)), [Ahuja and Mendoza \(1995\)](#) have found that as far as the far-field acoustics is concerned, for a cavity ratio of $L/W < 1$, the flow appears to be two dimensional (2D). For a cavity with $L/W > 1$, a 3D flow field is observed. Ahuja and Mendoza also found that the resonant frequencies are unaffected by the width of the cavity, but the amplitude of the sound pressure levels generated by 3D cavities is less than that for the 2D cases. Detailed experimental results on cavity noise have been compiled by [Ahuja and Mendoza \(1995\)](#) as benchmark cases for computational aeroacoustic (CAA) codes.

Shallow and Deep: The parameters that are used to define the shallow and deep Cavity regimes and their cut-off values are up for debate. According to [Sarohia \(1976\)](#) shallow cavities have length-to-depth (L/D) ratios less than 1.0 while deep cavities have L/D ratios greater than 1.0. [Rossiter \(1964\)](#) on the other hand, defined the cutoff to be a ratio of 4.0.

Open and Closed: Further classification of shallow cavities as Open, Closed, Transitionally open, and Transitionally closed at transonic and supersonic were identified by Stallings and Wilcox(1987) and Wilcox(1990).[The author was unable to find these papers cited by [Takeda and Shieh \(2004\)](#)].For very elongated cavities, the response is more broadband without clear self-sustaining phenomenon and hence called Closed.

2.3.2 Flow parameters

Mach number: In shallow cavities, where the feedback mechanism is usually dominant the higher Mach numbers generate louder noise levels throughout the entire spectrum. As a

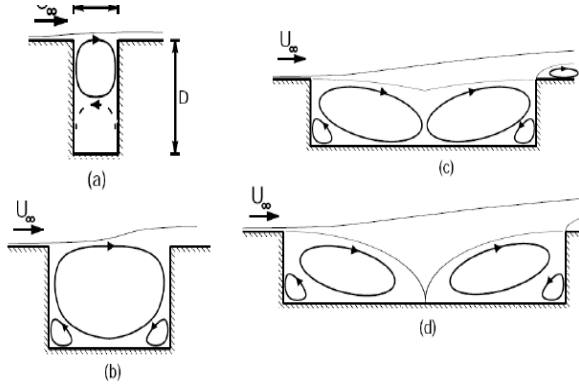


Figure 2.2: Schematic of deep (a) & shallow cavities: open (b), transitional (c), closed (d) (reproduced from Gloerfelt)

consequence, cavities at higher Mach numbers are more prone to nonlinear interactions, and higher-order harmonics are present. In very shallow cavities tones are usually not well defined, especially at low subsonic regime. On the other hand deep cavities may produce intense oscillations because of coupling with depth modes. The cavity flow in transonic and supersonic speeds will not be discussed as it is out of the scope of this project.

Boundary layer thickness: The ability of the shear layer to roll up into one or several vortices can determine the mode of oscillations at low Reynolds numbers. This roll-up mechanism is governed by the ratio of the cavity length over the momentum thickness of the separating boundary layer, L/δ_θ [Gharib and Roshko \(1987\)](#) and [Sarohia \(1976\)](#) found a minimum length L_m for the onset of oscillations. Below this length, the laminar shear layer cannot roll up.

Reynolds number: At low Reynolds number, Xavier Gloerfield argues in his review on Cavity Noise, the momentum thickness is determinant for the mode selection, since the overall shear layer rolls up as Kelvin-Helmholtz vortices. On the contrary, at sufficiently high Reynolds numbers ($Re_L > 10^6$), the size of the large vortex rolls is no more related with the Kelvin-Helmholtz instability, and the thickness of the incoming boundary layer has no incidence. Gloerfield also observed that, at high Reynolds numbers cavity flows are characterized by both broadband small-scales typical of turbulent shear layers, and discrete self-sustained oscillations due to a feedback phenomenon or a cavity resonance. In turbulent conditions, the coherent structures adopt the shape of clusters of small scales, and the alteration of different size of the dominant structures proceed by a reorganization of these clusters.

Shear-layer mode and wake mode: At low speeds, two different mode of flow has been observed. For the shear-layer mode, the shear layer spans the mouth of the cavity and stagnates at the aft wall. In this classification, the shear-layer mode can encompass both the fluid-dynamic and fluid-resonant regimes. The wake mode is identified by the stagnation of the flow prior to the aft wall (i.e., reattachment of the shear layer to the cavity base). Researchers such as [Gharib and Roshko \(1987\)](#) noted the flow looked similar to a bluffbody wake, hence the mode name. In the wake mode, self oscillations cease, the cavity flow "becomes unstable on a large scale", and the drag due to the presence of the cavity greatly increases.

In the early experimental work of Krishnamurty (1955), the acoustic fields produced by flow over 2D cavities were investigated with the Reynolds number per unit length varied from 0.214E6 to 0.3 14E6 for a Mach number range of 0.45-0.8. Using a spark Schlieren technique, it was observed that for turbulent boundary layer flow over cavities, the acoustic field was weaker and more diffuse than for that with a laminar boundary layer.

Chapter 3

Aeroacoustics

‘‘He conceived it in direct response to a technological need, honed it with a lovely balance of physical insight and mathematical rigour and described it in a style that remains today both a pleasure to read and a rich source of timeless information, each reading revealing new subtleties and depth’’
– J.E. Ffowcs Williams

3.1 Introduction

Aeroacoustics is a study of flow-induced noise, concerned with the sound generated by turbulent and/or unsteady vortical flows including the effects of any solid boundaries in the flow. It is clear from the previous chapter that much work had been done upon various matters concerning frequencies (such as showing that any frequencies in a fluid flow are equal to those of the sound generated) but the problem of estimating the intensity of the sound generated by a given flow was not seriously investigated.

Modern aeroacoustic science was pioneered in the 1950’s by Sir James Lighthill who, prompted by the need for quieter jet engines, derived an ‘*acoustic analogy*’ for the estimation of the intensity of sound radiated by a turbulent flow. Acoustic analogies are extensively used in Computational Aeroacoustics and will be used in this project in conjunction with Particle Image Velocimetry.

3.2 Sound and its properties

Sound may be defined as isentropic pressure-density perturbations in a fluid. These perturbations are often very small and propagate in a fluid at a speed given by

$$\begin{aligned} c_0 &= \sqrt{\left(\frac{\partial p}{\partial \rho}\right)_{s=s_0}} \\ &= \sqrt{\gamma R T} \quad \text{for ideal gas} \end{aligned}$$

where R is the gas constant, γ = ratio of specific heat of an ideal gas (C_p/C_v) and T the absolute temperature in Kelvin. The subscript $s = s_0$ indicates isentropic process.

3.3 Description of sound propagation using linear acoustics

Consider acoustic propagation as an isentropic perturbation of an equilibrium uniform reference state, described by the variables ρ_0 , p_0 and v_0 , the perturbed field variables can be rewritten as

$$\rho' = \rho - \rho_0 ; p' = p - p_0 ; v' = v - v_0$$

Assuming, $\rho \ll \rho_0$ and $p \ll p_0$, the governing equations of mass and momentum of ideal fluid can be linearized (Euler equations) and combined to obtain the well known wave equation :

$$\left(\frac{1}{c_0^2} \frac{\partial^2}{\partial t^2} - \nabla^2 \right) [(p - p_0) \delta_{ij}] = q(\mathbf{x}, t) \quad (3.1)$$

where, $q(x, t)$ as shorthand notation for the linear source term in the wave equation. In the absence of a source term, $q = 0$, the sound field is due to initial linear perturbations (or boundary conditions).

The propagation of sound can be described by D'Alembert's solution to wave equation

$$p' = F(\mathbf{n} \cdot \mathbf{x} - c_0 t) \quad (3.2)$$

where F is determined only when the initial boundary condition and the source term $q(\mathbf{x}, t)$ is known.

In order to determine the source $q(\mathbf{x}, t)$ from any measured acoustical field outside the source region, we need a physical model of the source. This is typical of any inverse problem in which the solution is not unique. A source can be modeled as a monopole (radially pulsating sphere) or a dipole (linearly translating sphere) or a quadrupole. When using microphone arrays to determine the sound sources responsible for aircraft noise one usually assumes that the sound field is built up of monopole sound sources.

Predicting the noise radiation associated with unsteady flows is the central theme of aeroacoustics. The true nature of these sources can not be accurately described by the linear theory as majority of sound production is due to non-linear fluid motions and fluid-structure interactions.

3.4 Computational aeroacoustics

A variety of approaches are available to compute the flow data and to estimate the radiated noise from the flow. Computational techniques for flow-generated sound can be classified into two broad categories:

- Direct approaches
- Hybrid approaches

3.4.1 Direct approaches

The direct approach computes the sound together with its fluid dynamic source field by solving the compressible flow equations. The direct computation of sound using DNS is restricted to low Reynolds numbers and simple geometries due to large computational time and memory required. Therefore, it is more suitable for producing benchmark databases or developing theoretical models, rather than to predict the sound emission of an aeroacoustic problem. In their review, [Colonius and Lele \(2004\)](#) has identified many limitations of Direct Approaches.

3.4.2 Hybrid approaches

In a hybrid approach, the computation of flow (source) is decoupled from the computation of sound (propagation) by a flow-field decomposition. Turbulent noise source field is computed and/or modeled using the tools mentioned in the Direct Approaches. The far-field propagations can then be obtained by linearized model like Linearized Euler equations using a coarser mesh. However, computational domain is still large because it must include the source field and at least a part of the acoustic near field, leading to a large computational costs. Alternatively, computation of sound from the sources can be done in a post-processing step using scalar equations based on an aero-acoustic theory(or analogy) discussed later in this chapter.

3.5 Experimental aeroacoustics

3.5.1 Particle Image Velocimetry and Acoustic Analogy

Particle image velocimetry (PIV) is an optical experimental technique for fluid visualization. It is used to obtain instantaneous velocity measurements and related properties in fluids. In recent years, staggering improvements in the performance of high-resolution & high-speed cameras and powerful lasers has made Time resolved Particle Image Velocimetry an increasingly popular technology as an alternative to hybrid techniques in Computational Aeroacoustics. TR-PIV can be used to obtain space-time history of a flow field (velocity and pressure fields) in a flow. The noise at far-field can be easily estimated using an appropriate Acoustic Analogy. This method can be thus considered as a Hybrid approach.

3.5.2 Microphones

A microphone is an acoustic-to-electric transducer, or sensor, that converts sound into an electrical signal. Simultaneous use of arrays of microphones in conjunction with beamforming algorithms allow for both the quantification and the spatial localization of the acoustic sources. However, they do not provide any knowledge of the nature of these sources and mechanism of sound production. In this project microphones are used for validation of acoustic prediction from TR-PIV.

3.6 Aeroacoustic analogies

Consider, a flow solution \mathbf{q} (a vector of velocities and thermodynamic variables sufficient to uniquely define a flow condition) satisfying the compressible flow equations:

$$N(\mathbf{q}) = 0 \quad (3.3)$$

Part of \mathbf{q} is sound, but without the benefits of scaling or other firm arguments its mathematical definition remains vague. Also, solving the flow equations using direct methods (and most hybrid methods) will not provide any information on location of sound generation and its mechanism. The scalar equation from acoustic analogies, however makes this possible.

An acoustic analogy may be formulated by rearranging eq (3.3) into

$$L(\mathbf{q}) = S(\mathbf{q}) \quad (3.4)$$

where, L is some (usually linear) wave propagation operator. $S(\mathbf{q})$ is then its corresponding nominal (nonlinear) forcing term, which can be assumed to act, analogous to an externally applied source, \mathbf{q} on an quiescent flow (or reference flow), \mathbf{q}_0 . The difference between the actual flow, and the reference flow $\mathbf{q}_0 - \bar{\mathbf{q}}$ is identified as a source of sound.

$$L(\mathbf{q} - \mathbf{q}_0) = S(\bar{\mathbf{q}} - \mathbf{q}_0)$$

This decomposition, whatever motivates the particular form of L and S , accurately describes the small (linear) acoustic perturbations in quiescent reference fluid surrounding away from the source, if L can somehow be inverted (e.g. using Green's Functions) to provide \mathbf{q} in the far field where it is purely acoustic.

The acoustic analogy was first introduced by [Lighthill \(1952\)](#) and was extended by [Curle \(1955\)](#) and [Ffowcs Williams \(1969\)](#) to include the effects of solid surfaces in arbitrary motion.

The acoustic analogy can give prediction of sound at far field only when space-time history of the flow field, $\bar{\mathbf{q}}$ is known or has been determined by time-accurate turbulence simulation tools (such as DNS, LES, and unsteady RANS methods) or by experiments (PIV).

3.7 Lighthill's analogy

[Lighthill \(1952\)](#) pioneered the field of aeroacoustic by deriving the true nature of sound sources in a turbulent flow. He achieved this by re-arranging the Navier-Stokes equations, which govern the flow of a compressible viscous fluid, without any simplifications, into an inhomogeneous differential wave equation, thereby making a connection between fluid mechanics and acoustics. Lighthill's equation is given by :

$$\frac{\partial^2 \rho}{\partial t^2} - c_0^2 \nabla^2 \rho = \frac{\partial^2 T_{ij}}{\partial x_i \partial x_j}, \quad (3.5)$$

where,

$$T_{ij} = \rho v_i v_j - \sigma_{ij} + (p - c_0^2 \rho) \delta_{ij} \quad (3.6)$$

is the so-called Lighthill turbulence stress tensor for the acoustic field. It is important to realize that Lighthill's equation is exact in the sense that no approximations of any kind have been made in its derivation.

Lighthill asserted that the sound generated by the turbulence in the real fluid is exactly equivalent to that produced in an ideal, stationary acoustic medium forced by a stress distribution represented by the nonlinear tensor T_{ij} . Thus, we no more assume that the flow in the source region is a linear perturbation of the reference state. This is known as Lighthill's Analogy.

Each of the acoustic source terms, i.e. terms in T_{ij} , may play a significant role in the generation of noise depending upon flow conditions considered. $\rho v_i v_j$ describes unsteady convection of flow (or Reynold's Stress), σ_{ij} describes sound generated by shear, and $(p - c_0^2 \rho) \delta_{ij}$ describes non-linear acoustic generation processes.

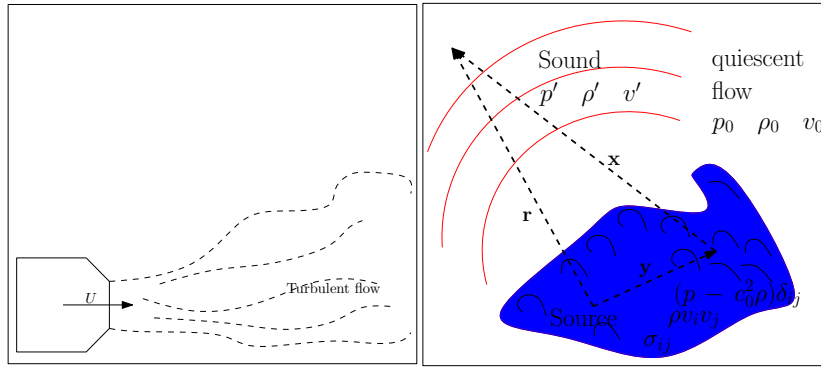


Figure 3.1: Lighthill's Analogy for a Turbulent Jet

The formal solution of Lighthill's equation (3.5) with outgoing wave behavior is given by

$$c_0^2(\rho - \rho_0)(\mathbf{x}, t) = \frac{1}{4\pi} \frac{\partial^2}{\partial x_i \partial x_j} \int_{-\infty}^{\infty} \frac{T_{ij}(\mathbf{y}, t - |\mathbf{x} - \mathbf{y}|/c_0)}{|\mathbf{x} - \mathbf{y}|} d^3\mathbf{y} \quad (3.7)$$

where, T_{ij} is given by 3.6

3.8 Curle's analogy

In most applications of Lighthill's theory it is necessary to generalize the solution (3.7) to account for the presence of solid bodies in the flow. Indeed, noise is frequently generated in the boundary layers and wakes of flow past such bodies (airfoils, cavity) and the unsteady surface forces (dipoles) that arise are likely to make significant contribution to the production of sound.

To account for these boundary effects, Curle derived an analogy more fundamentally, by considering the most general solution to equation (3.5) which is the well known

$$\rho - \rho_0 = \frac{1}{4\pi c_0^2} \int_V \frac{\partial^2 T_{ij}}{\partial y_i \partial y_j} \frac{d\mathbf{y}}{|\mathbf{x} - \mathbf{y}|} + \frac{1}{4\pi} \int_S \left\{ \frac{1}{r} \frac{\partial \rho}{\partial n} + \frac{1}{r^2} \frac{\partial r}{\partial n} \rho + \frac{1}{c_0 r} \frac{\partial r}{\partial n} \frac{\partial \rho}{\partial t} \right\} dS(\mathbf{y}) \quad (3.8)$$

where the integrands are evaluated at retarded times $t - r/c_0$, where $r = |\mathbf{x} - \mathbf{y}|$

By applying divergence theorem twice to the volume integral and substituting the expression for T_{ij} from 3.6, Curle derived the fundamental result of his paper.

$$\begin{aligned}\rho(\mathbf{x}, t) - \rho_0 &= \frac{1}{4\pi c_0^2} \frac{\partial^2}{\partial x_i \partial x_j} \int_V \frac{T_{ij}(\mathbf{y}, t - \frac{r}{c_0})}{r} dV(\mathbf{y}) + \frac{1}{4\pi c_0^2} \frac{\partial}{\partial x_i} \int_S \frac{1}{r} n_j p_{ij} dS(\mathbf{y}) \\ &= \frac{1}{4\pi c_0^2} \frac{\partial^2}{\partial x_i \partial x_j} \int_V \frac{T_{ij}(\mathbf{y}, t - \frac{r}{c_0})}{r} dV(\mathbf{y}) - \frac{1}{4\pi c_0^2} \frac{\partial}{\partial x_i} \int_S \frac{P_i(\mathbf{y}, t - \frac{r}{c_0})}{r} dS(\mathbf{y})\end{aligned}\quad (3.9)$$

where,

$$P_i = -n_j p_{ij} \quad (3.10)$$

P_i is exactly the force per unit area exerted on the fluid by solid boundaries in x_i direction. It must be pointed out again that, just as in Lighthill's theory, the above analysis by Curle's Analogy is exact and no simplifying assumptions have been made so far.

Curle (1955) observed that solid boundaries could make their presence felt in two ways :

1. The sound generated by the quadrupoles(distributed throughout the region external to the solid boundaries) will be reflected and diffracted by the solid boundaries
2. There might be a resultant distribution of dipoles (or even sources) at the boundaries.

3.9 Modified Curle's Equation with Simplifying Assumptions

3.9.1 Basic assumptions:

Although Curle's Analogy is exact and no simplifying assumptions have been made, three important assumptions are implicitly made while implementing the analogy to turbulent flows.

Assumption 1 Source Term (T_{ij}) do not depend on acoustic field

Assumption 2 Isotropic wave operator describes the propagation of sound accurately

Assumption 3 Observer is located in a region where flow is isentropic

Mathematically, the first assumption cannot be true because the density term appears on the both sides of the equation. Physically speaking, sound is produced by Hydrodynamic phenomenon which are almost independent of acoustic phenomenon. Moreover, PIV captures the actual flow in which these cross-interferences have already been incorporated.

The second assumption is true only for the regions where the flow is stagnant ie. zero. In low mach number flows, which is true for our case as well, the second assumption is a good approximation, since the convection effects are a factor M slower than the propagation of the acoustic wave.

The mathematical significance of third assumption is that the density fluctuations can be written as

$$\rho(\mathbf{x}, t) - \rho_0 = (p(\mathbf{x}, t) - p_0)/c_0 \quad (3.11)$$

Thus,

$$p(\mathbf{x}, t) - p_0 = \frac{1}{4\pi c_0} \frac{\partial^2}{\partial x_i \partial x_j} \int_V \frac{T_{ij}(\mathbf{y}, \tau)}{r} dV(\mathbf{y}) + \frac{1}{4\pi c_0} \frac{\partial}{\partial x_i} \int_S \frac{n_j p_{ij}(\mathbf{y}, \tau)}{r} dS(\mathbf{y}) \quad (3.12)$$

where $\tau = t - r/c_0$, $r = |\mathbf{x} - \mathbf{y}| = \sqrt{x_i^2 - y_i^2}$

3.9.2 Spatial derivative to temporal derivative

When computing the solution of Curle's Analogy numerically, it is favorable to transform spatial derivatives into temporal ones. The reason is that the temporal form of the solution is less sensitive to numerical errors. [Larsson et al. \(2004\)](#) converted the spatial derivative into temporal one by applying the chain rule :

$$\frac{\partial f(\tau)}{\partial x_i} = \frac{\partial f}{\partial \tau} \frac{\partial \tau(r)}{\partial x_i} = \frac{\partial f}{\partial \tau} \left(-\frac{1}{c_0} \frac{\partial r(x_i)}{\partial x_i} \right) = \frac{\partial f}{\partial \tau} \left(-\frac{l_i}{c_0} \right) \quad (3.13)$$

to obtain ,

$$\begin{aligned} p((x), t) - p_0 &= \frac{1}{4\pi} \int_V \left[\frac{l_i l_j}{c_0^2 r} \ddot{T}_{ij} + \frac{3l_i l_j - \delta_{ij}}{c_0 r^2} \dot{T}_{ij} + \frac{3l_i l_j - \delta_{ij}}{r^3} T_{ij} \right] dV(\mathbf{y}) \\ &\quad + \frac{1}{4\pi} \int_S l_i n_j \left[\frac{\dot{p}\delta_{ij} - \ddot{\tau}_{ij}}{c_0 r} + \frac{p\delta_{ij} - \tau_{ij}}{r^2} \right] dS(\mathbf{y}) \end{aligned} \quad (3.14)$$

where, $l_i = (x_i - y_i)/r$ = unit vector directed from the source point, \mathbf{y} to listener, \mathbf{x}

3.9.3 Simplifying assumptions

Assumption 5 Viscous effects are insignificant

Assumption 6 Flow is Isothermal(or Isentropic) in the flow

Assumption 7 Compressibility effect are negligible in the flow

[Lighthill \(1952\)](#) observed that, in practice the dissipation of acoustic energy into heat, by viscosity and heat conduction, is a slow process. The contribution of the viscous stresses to τ_{ij} is therefore probably unimportant, at least for phenomena on a terrestrial scale of distance. Near the walls, on the other hand, viscous tangential stresses and entropy variations play an important role. However, in real configurations, these phenomena are usually overwhelmed by the normal stresses and generally neglected

For flows in which the temperature departs little from uniformity the differences between the exact pressure field, $p\delta_{ij}$ and the approximate one $c_0^2 p_{ij}$ are similarly unimportant.

Then the principal generators of sound are the fluctuating Reynolds stresses, $\rho v_i V_j$ corresponding to variable rates of momentum flux across surfaces fixed in the fluctuating fluid flow. Mathematically, these assumptions imply that

$$T_{ij} = \rho v_i v_j \quad (3.15)$$

In fact, [Larsson et al. \(2004\)](#) have concluded (CAA) that the common simplification $T_{ij} = \rho v_i v_j$ is valid and introduces very small errors at low mach numbers.

The solution to Curle's Analogy now reduces to

$$\begin{aligned} p((x), t) - p_0 &= \frac{1}{4\pi} \int_V \left[\frac{l_i l_j}{c_0^2 r} \frac{\partial^2}{\partial t^2} (\rho v_i v_j) + \frac{3l_i l_j - \delta_{ij}}{c_0 r^2} \frac{\partial}{\partial t} (\rho v_i v_j) + \frac{3l_i l_j - \delta_{ij}}{r^3} (\rho v_i v_j) \right]_{\tau=t-r/c_0} dV(\mathbf{y}) \\ &\quad + \frac{1}{4\pi} \int_S l_i n_j \left[\frac{1}{c_0 r} \frac{\partial}{\partial t} (p \delta_{ij}) + \frac{p \delta_{ij}}{r^2} \right]_{\tau=t-r/c_0} dS(\mathbf{y}) \end{aligned} \quad (3.16)$$

3.9.4 Acoustic compactness

In general, a body is said to be acoustically compact when its characteristic dimension is small compared to the wavelengths of the sound waves it is producing or with which it interacts.

$$\frac{L}{\lambda} = \frac{\kappa_0 L}{2\pi} \ll 1$$

Assumption 8 Compact Body Assumption

Consider the case of cavity flow, where its length, L is the characteristic length, free velocity, U is the characteristic velocity and it can be found from microphone data that the Strouhal Number (St) scales with unity.

$$\begin{aligned} St &= \frac{f L}{U} \sim 1 \Rightarrow f \sim \frac{U}{L} \Rightarrow \lambda = \frac{c_0}{f} \sim \frac{c_0 L}{U}; \\ \lambda &\sim \frac{L}{M} \Rightarrow \frac{L}{\lambda} \ll 1 \Rightarrow \text{Cavity Flow is acoustically compact source} \end{aligned}$$

If the compactness condition is satisfied, we can neglect the variations of retarded time, τ over the surface. Mathematically, it implies that

$$\tau = t - |\mathbf{x}|/c_0 \quad \forall \mathbf{y} \in \Omega \quad (3.17)$$

if we chose the origin $\mathbf{y} = 0$ inside or near the body. Under this assumption the solution to Curle's Analogy can be simplified to :

$$\begin{aligned} p((x), t) - p_0 &= \frac{1}{4\pi} \left[\int_V \left(\frac{l_i l_j}{c_0^2 r} \frac{\partial^2}{\partial t^2} (\rho v_i v_j) + \frac{3l_i l_j - \delta_{ij}}{c_0 r^2} \frac{\partial}{\partial t} (\rho v_i v_j) + \frac{3l_i l_j - \delta_{ij}}{r^3} (\rho v_i v_j) \right) dV(\mathbf{y}) \right]_{\tau=t-|\mathbf{x}|/c_0} \\ &\quad + \frac{1}{4\pi} \left[\int_S \left(l_i n_j \frac{1}{c_0 r} \frac{\partial}{\partial t} (p \delta_{ij}) + \frac{p \delta_{ij}}{r^2} \right) dS(\mathbf{y}) \right]_{\tau=t-|\mathbf{x}|/c_0} \end{aligned} \quad (3.18)$$

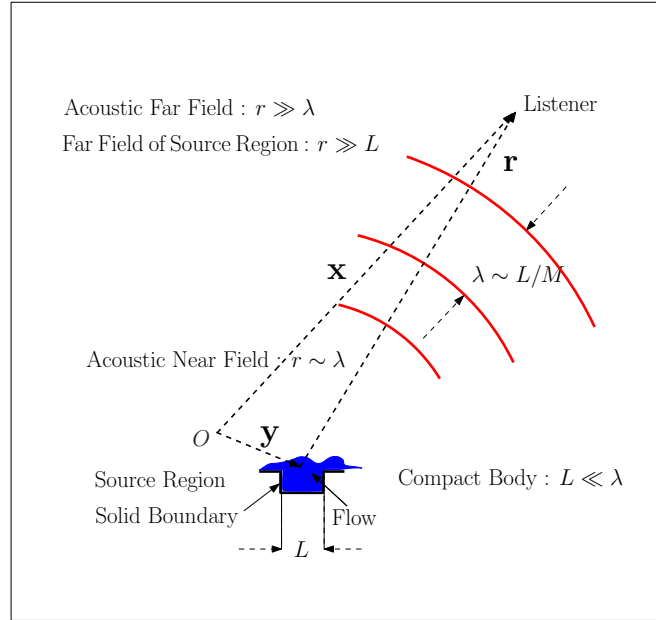


Figure 3.2: Schematic of source and sound scales

3.9.5 Efficiency of Sources

Let us compare the order of magnitude of sound (ρ') due to volumetric sources, ($V1, V2, V3$) and surface sources, ($S1, S2, S3$) :

$$\begin{aligned} \rho((x), t) - \rho_0 = \frac{1}{4\pi c_0^2} & \left[\int_V \left(\underbrace{\frac{l_i l_j}{c_0^2 r} \frac{\partial^2}{\partial t^2} (\rho v_i v_j)}_{V1} + \underbrace{\frac{3l_i l_j - \delta_{ij}}{c_0 r^2} \frac{\partial}{\partial t} (\rho v_i v_j)}_{V2} + \underbrace{\frac{3l_i l_j - \delta_{ij}}{r^3} (\rho v_i v_j)}_{V3} \right) dV(\mathbf{y}) \right]_{\tau=t-|\mathbf{x}|/c_0} \\ & + \frac{1}{4\pi} \left[\int_S l_i n_j \left(\underbrace{\frac{1}{c_0 r} \frac{\partial}{\partial t} (p \delta_{ij})}_{S1} + \underbrace{\frac{p \delta_{ij}}{r^2}}_{S2} \right) dS(\mathbf{y}) \right]_{\tau=t-|\mathbf{x}|/c_0} \end{aligned} \quad (3.19)$$

We assume that the frequency of sound production scales with U/L (which we see later, is true for cavity flow) so that time, t scales with L/U .

Sound from Volumetric Sources (V1, V2, V3) : Reynold's stress terms $\rho v_i v_j$ scales with $\rho_0 U^2$ and their time derivatives scale with $(U/L)\rho_0 U^2$ and $(U/L)^2 \rho_0 U^2$ respectively.

$$[\rho']_{V1} \sim \frac{1}{c_0^2} \frac{1}{c_0^2} \frac{1}{R} \left(\frac{U}{L} \right)^2 \rho_0 U^2 L^3 = \frac{U^4}{c_0^4} \frac{\rho_0 L}{R}$$

The density variation then scale as

$$[\rho']_{V1} \sim \rho_0 \left(\frac{U}{c_0} \right)^4 \frac{L}{R} = \rho_0 M^4 \left(\frac{L}{R} \right)$$

similarly,

$$\begin{aligned} [\rho']_{V2} &\sim \rho_0 \left(\frac{U}{c_0} \right)^3 \frac{L^2}{R} = \rho_0 M^3 \left(\frac{L}{R} \right)^2 \\ [\rho']_{V3} &\sim \rho_0 \left(\frac{U}{c_0} \right)^2 \frac{L^3}{R} = \rho_0 M^2 \left(\frac{L}{R} \right)^3 \end{aligned} \quad (3.20)$$

Sound from Surface Sources (S1, S2) : The thermodynamic pressure, p scales with $\rho_0 U^2$ and its fluctuation, $\frac{\partial}{\partial t}(p\delta_{ij})$ scales with $(U/L)\rho_0 U^2$. Thus, it may be concluded from surface integral of eq (3.19), the sound(ρ') at a distance R is

$$\begin{aligned} [\rho']_{S1} &\sim \frac{1}{c_0^2} \frac{1}{c_0} \frac{1}{R} \left(\frac{U}{L} \right) \rho_0 U^2 L^2 = \rho_0 \frac{U^3}{c_0^3} \left(\frac{L}{R} \right) \\ [\rho']_{S1} &\sim \rho_0 \left(\frac{U}{c_0} \right)^3 \left(\frac{L}{R} \right) = \rho_0 M^3 \left(\frac{L}{R} \right) \end{aligned}$$

similarly,

$$[\rho']_{S2} \sim \rho_0 \left(\frac{U}{c_0} \right)^2 \left(\frac{L}{R} \right)^2 = \rho_0 M^2 \left(\frac{L}{R} \right)^2 \quad (3.21)$$

3.9.6 Near field sound predictions

Near field may be defined as the locations whose distance from the source scale with the wavelength of the sound, ie.

$$R \sim \lambda$$

but, for cavity flow (see section 3.9.4):

$$\begin{aligned} \lambda &\sim \frac{L}{M} \\ \Rightarrow R &\sim \frac{L}{M} \quad \Rightarrow \frac{L}{R} \sim M \end{aligned} \quad (3.22)$$

Assumption 9 Volumetric (quadrupole) sources inefficient compared to surface (dipole) sources

For near field sound computations from a cavity flow, L/R scales with M . Using this condition in equations (3.20 and 3.21) it can be easily found that the sound from volumetric sources in a cavity flow scale with M^5 , while the sound due to surface sources scale with M^4

$$\begin{aligned} [\rho']_{V1,V2,V3} &\sim \rho_0 M^5 \\ [\rho']_{S1,S2} &\sim \rho_0 M^4 \\ \Rightarrow [\rho']_{volume} &\ll [\rho']_{surface} \end{aligned}$$

Under this assumption , the solution to Curle's analogy reduces to

$$p((x), t) - p_0 = \frac{1}{4\pi} \left[\int_S l_i n_j \left(\frac{1}{c_0 r} \frac{\partial}{\partial t} (p \delta_{ij}) + \frac{p \delta_{ij}}{r^2} \right) dS(\mathbf{y}) \right]_{\tau=t-|\mathbf{x}|/c_0} \quad (3.23)$$

The main source of sound generation in a low Mach number cavity flow is the interaction of the flow with the cavity walls. Specifically, the vortices shed from the cavity leading edge create pressure fluctuation when they impinge onto the cavity forward facing step. These surface pressure fluctuations make the surface integral contribution to farfield noise dominant with respect to that of the volume integral.

3.9.7 Far field sound prediction

Near field may be defined as the location of listener whose distance from the source is many times wavelength of the sound, ie.

$$R \sim N\lambda$$

where, N is a large value

but, for cavity flow (see section 3.9.4):

$$\begin{aligned} \lambda &\sim \frac{L}{M} \\ \Rightarrow \frac{R}{N} &\sim \frac{L}{M} \quad \Rightarrow \frac{L}{R} \sim \frac{M}{N} \end{aligned} \quad (3.24)$$

For near field sound computations from a cavity flow, L/R scales with M/N . Using this condition in equations (3.20 and 3.21) it can be easily found that

$$\begin{aligned} [\rho']_{S1} &\sim \rho_0 M^3 \frac{M}{N} \sim \rho_0 \frac{M^4}{N} \\ [\rho']_{S2} &\sim \rho_0 M^2 \left(\frac{M}{N} \right)^2 \sim \rho_0 \frac{M^4}{N^2} \\ \Rightarrow [\rho']_{S2} &\ll [\rho']_{S1} \end{aligned}$$

Assumption 10 Neglect second integral term in equation 3.23

$$p((x), t) - p_0 = \frac{1}{4\pi c_0} \int_S \frac{l_i n_j}{r} \frac{\partial}{\partial t} (p \delta_{ij}) dS(\mathbf{y}) \quad (3.25)$$

3.9.8 Gutin's principle

The time integral maybe taken out of the spatial integration so that it reduces to time-derivative of surface integral of pressure.

$$p((x), t) - p_0 = \frac{l_i}{4\pi c_0 r} \frac{\partial}{\partial t} F_j(\tau) \quad (3.26)$$

where, $F_j(\tau) = \int_S n_j(p\delta_{ij})dS(\mathbf{y})$ can be interpreted as total force exerted by the fluid on the body. Equation (3.26) is the analytical expression of the so called Gutin's principle for compact rigid bodies, which directly relates the force F_j exerted by the fluid on the body to the radiated field, in a far field approximation.

3.10 Implementation of acoustic analogy to cavity flow

The main purpose of the present investigation is the computation of the acoustic pressure signal in the acoustic far-field, based on the experimental flow data, and its comparison with the measurements of the four far-field microphones.

3.10.1 Analytical Formulations

At the low Mach number of the present experiment ($M < 0.05$), relatively high Reynolds number ($Re > 10,000$) and far-field location for the acoustic evaluation, the following simplifying assumptions were made, as discussed in Chapter(Acoustic Analogy) :

Haigermoser (2009) suggested that since, pressure fields obtained from the PIV data are only available in a $2D$ plane, the above equation is integrated in the out-of-plane direction from $-w$ to w , where w is half the cavity spanwise extension, yielding an integral solution which will henceforth be called **Curle's Analogy** :

$$p((x), t) - p_0 = \frac{1}{4\pi} \int_L l_i n_j \left[2 \tan^{-1} \left(\frac{w}{r} \right) \frac{\dot{p}\delta_{ij}}{c_0} + 2w \frac{p\delta_{ij}}{r^2} \right]_{\tau=t-|\mathbf{x}|/c_0} dL(y) \quad (3.27)$$

The dimensional analysis of the two surface integral terms suggest that the contributions of both terms are significant in the near field. However, the efficiency of the second term decreases rapidly in far-field and can be neglected to obtain **Gutin's Principle**:

$$p((x), t) - p_0 = \frac{l_i}{4\pi c_0 r} \frac{\partial}{\partial t} F_j(\tau) \quad (3.28)$$

where,

$$F_j(\tau) = \int_S n_j(p\delta_{ij})dS(\mathbf{y})$$

can be interpreted as total force exerted by the fluid on the body.

3.10.2 Numerical Implementation

In this project, the Curle acoustic analogy [equation(3.27)], Gutin's Principle [equation(3.26)] has been implemented to compute acoustic field. The time history of 2D pressure fields is obtained from the post processing of PIV data and Planar Pressure Imaging (PIV-PPI) which is described in the next chapters. The pressure time derivative is calculated with a second-order central difference scheme. The surface integral is truncated due to the limited field of view, meaning that sound sources which are lying outside the field of view are not considered.

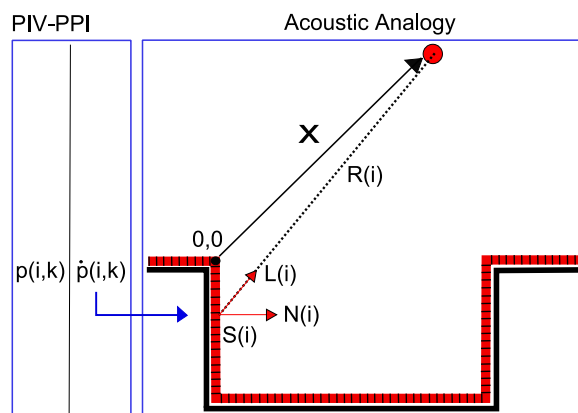


Figure 3.3: Implementation of acoustic analogy from data generated from PIV-PPI

The origin was set to coincide with the leading edge of the cavity. For each spatial location of listener in the acoustic field \mathbf{x} in the acoustic field and time instant, k sound pressure, $SP(\mathbf{x}, k)$ was computed by a discretized integral over the cavity surface for each pressure field obtained from PIV-PPI. The integral is computed by means of trapezoidal rule.

$$SP(\mathbf{x}, k) = \frac{1}{4\pi} \sum_i^n \left[L(i) \cdot N(i) \left(2 \tan^{-1} \left(\frac{w}{R(i)} \right) \frac{\dot{p}(i, k)}{c_0} + 2 w \frac{p(i, k)}{R(i)^2} \right) \right] \Delta S(i) \quad (3.29)$$

where $R(i)$ is the distance of the surface element $S(i)$ from the listener in the acoustic field. The time history sound pressure in the acoustic field was stored in a sound pressure matrix $SP(x, y, k)$. Spectral and statistical analysis was performed on the sound data to obtain useful results.

Chapter 4

Particle Image Velocimetry

One of the most successful experimental techniques that emerged in the past decades is Particle Image Velocimetry. PIV is a non-intrusive, quantitative flow visualization technique which allows measurement of instantaneous velocity field within a plane (and recently extended to a three-dimensional volume within the flow domain).

The principle of PIV is based on the measurement of the displacement of small tracer particles that are carried by the fluid during a short time interval. The tracer particles must be sufficiently small to accurately follow the fluid motion and not alter the fluid properties or flow characteristics. A schematic of a typical experimental set-up for PIV is shown in the figure below.

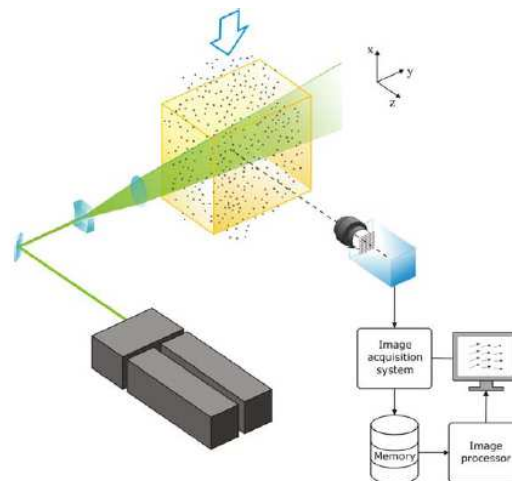


Figure 4.1: Schematic of a typical PIV measurement system

The tracer particles are illuminated within a thin light sheet generated from a pulsed light source (usually a double-head pulsed laser system), and the light scattered by them is recorded onto two subsequent image frames by a digital imaging device, typically a CCD camera placed perpendicular to the measurement plane.

The recorded images are typically analyzed off-line on a digital computer although modern computers enable an on-line visualization of PIV measurements at a rate of approximately one

velocity field per second (based on 1 Megapixel images). This consists essentially of a cross-correlation analysis of the particle-image patterns in small sub-domains called interrogation windows, between the first and second image frame. The particle-image pattern displacement divided by the image magnification and the time delay between the laser light pulses yields the local fluid velocity. This process is repeated for the entire image domain, which yields the instantaneous velocity in a planar cross-section of the observed flow. Sophisticated interrogation methods have been developed that make it possible to interrogate images at high spatial resolution and to determine displacements with high accuracy.

4.1 Parameters which influence PIV measurements :

4.1.1 Flow Seeding

It is clear from the principle of PIV, that the measurement technique is indirect as it determines the particle velocity instead of the fluid velocity. Therefore, fluid mechanical properties of the particles have to be examined in order to avoid significant discrepancies between fluid and particle motion.

Assuming spherical particles in a viscous fluid at a very low Reynolds number the velocity lag of a particle in a continuously accelerating fluid can be derived using Stkokes' drag law :

$$\mathbf{U}_s = \mathbf{U}_p - \mathbf{U} = d_p^2 \frac{(\rho_p - \rho)}{18\mu} \mathbf{a} \quad (4.1)$$

where,

- \mathbf{U}_s = velocity lag,
- \mathbf{U}_p = particle velocity
- \mathbf{U} = fluid velocity,
- d_p = particle diameter,
- ρ_p = particle mass density,
- ρ = fluid mass density,
- μ = dynamic viscosity of fluid

The step response of U_p typically follows an exponential law if the density of the particle is much greater than the fluid density:

$$\mathbf{U}_p(t) = \mathbf{U} \left[1 - \exp \left(\frac{-t}{\tau_s} \right) \right] \quad (4.2)$$

where,

$$\tau_s = d_p^2 \frac{\rho_p}{18\mu} \quad (4.3)$$

τ_s remains a convenient measure for the tendency of particles to follow fluid motion.

From equation (4.3) it can be seen that due to the difference in density between the fluid and the tracer particles, the diameter of the particles should be very small in order to ensure good tracking of the fluid motion. On the other hand, the particle diameter should not be too small as light scattering properties have also to be taken into account as will be shown in the following section.

Further, the seeding density should be homogeneous. Typical seeding concentration applied in aerodynamic flows is 10 particles/mm³

The particle tracers need to be illuminated and observed twice within the time separation. In general it can be said that the light scattered by small particles is a function of the ratio of the refractive index of the particles to that of the surrounding medium, the particles size, their shape and orientation. Furthermore, the light scattering also depends on polarization and observation angle. For spherical particles with diameters, d_p , larger than the wavelength of the incident light λ , Mies scattering theory can be applied.

Light scattering patterns, according to Mie's theory, are shown in Figure (4.2) for decreasing wavelengths. The intensity scales are in logarithmic scale and are plotted so that the intensity for neighboring circles differ by a factor of 100. It would be advantageous to record in forward scatter since the intensity obtained will be highest. However, due to the limited depth of field, recording at 90° . is most often used. Although, larger particles and number density of particles could be used to increase scattering efficiency but they also generate more noise.

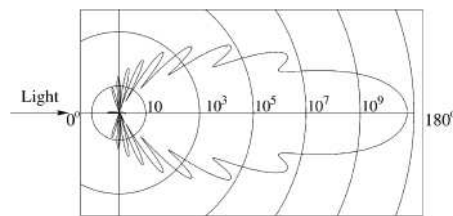


Figure 4.2: Scattering directivity of tracer particles

4.1.2 Illumination

Lasers are widely used in PIV, because they fulfill the following requirements

1. The first requirement for a light source suited for PIV experiments is the short duration of illumination. A practical criterion for the choice of the maximum duration of each illumination pulse is that particle images do not appear as streaks but rather as circular dots.
2. The second requirement is that only the particles lying within a thin light sheet are illuminated such that they can all be imaged in focus.
3. the intensity of the light source must allow the scattered light from the seeding particles to be detected by digital imaging devices.

Lasers can emit monochromatic light with high energy density, which can easily be bundled into thin light sheets for illuminating and recording the tracer particles without chromatic aberrations. The most common device used for PIV experiments is the solid-state frequency-doubled Neodym:YAG laser (Nd:YAG) that emits light with a wavelength of 532 nm. It produces pulse energy ranging between 10 mJ and 1 J. With the very short pulse duration (between 5 ns and 15 ns) this instrument is practically suited to illuminate flows without any limit on the flow speed. The standard architecture of a PIV laser consists of two separate lasers firing independently at the required pulse separation. Therefore the time separation can be freely optimized for the experimental conditions, primarily the flow speed and the imaging magnification.

4.1.3 Light Sheet Formation Optics

The circular cross section beam delivered by the light source is shaped into a thin sheet by means of cylindrical and spherical lenses. Common arrangements are illustrated in Figure 9.11. In order to minimize the variation of the light sheet properties within the area of interest it is convenient to design the light sheet optics in such a way that the beam waist does not fall within the measurement region.

An important parameter governing the quality of the illumination is the overlap between the two thin light sheets formed by the two lasers (in case of dual head Nd:YAG). Light sheets

poor overlap is among the first reason for unsuccessful or poor quality experiments. Therefore a careful relative alignment of the two laser sheets is needed in order to achieve an acceptable level of overlap typically of about 80

4.1.4 Particle Image Formation Optics

A schematic of the PIV optical configuration is shown in Figure 4.3. An image of the tracer particles in the light sheet is formed by means of a lens on the surface of an image sensor. The imaging system is characterized by its focal length f , f-number (or f-stop), $f/\#$ and image magnification M defined as the ratio of the image distance d_i and object distance d_o , as described by the lens equation:

$$\frac{1}{f} = \frac{1}{d_i} + \frac{1}{d_o} ; \quad M = \frac{d_i}{d_o} ; \quad f/\# = f/D \quad (4.4)$$

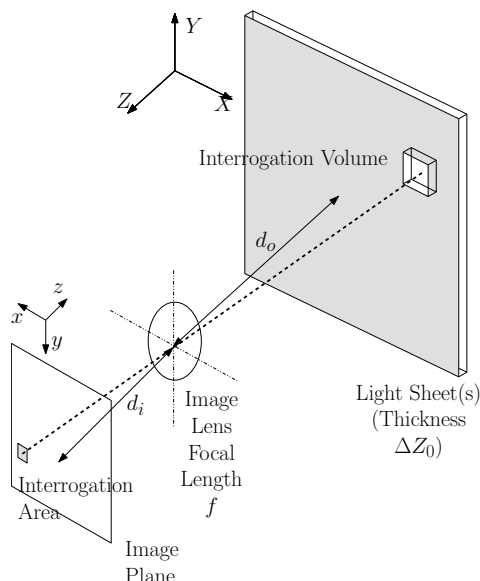


Figure 4.3: Schematic of PIV optics

The image diameter of a spherical tracer particle formed due geometric optics as described above can be estimated as

$$d_{geom} = d_p M \quad (4.5)$$

The image diameter of the spherical tracer particle formed due to diffraction effect can be estimated as

$$d_{diff} = 2.44\lambda(1 + M)f/\# \quad (4.6)$$

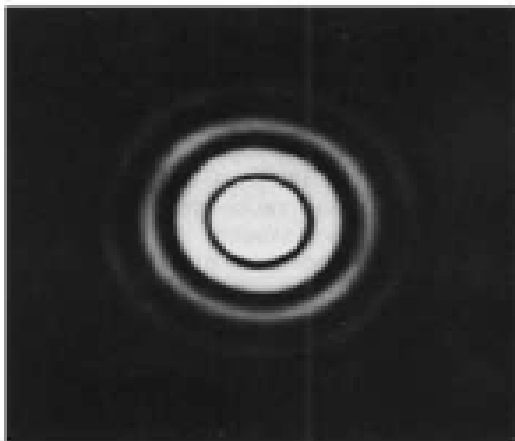
An acceptable approximation of the resulting particle image diameter is given by the Euclidean sum of the above terms:

$$d_\tau = \sqrt{(d_{geom})^2 + (d_{diff})^2} \quad (4.7)$$

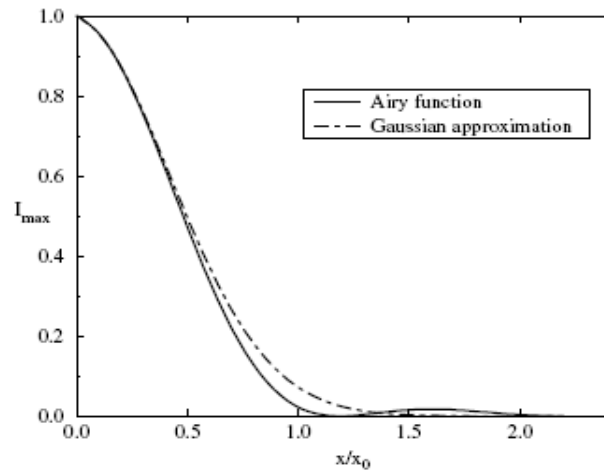
For typical optical parameters in PIV, it is concluded that $d_{diff} \gg d_{geom}$ and therefore

$$\begin{aligned} d_\tau &\simeq d_{diff} \\ &= 2.44\lambda(1 + M)f/\# \end{aligned} \quad (4.8)$$

In other words, the diffraction limit generally dominates the particle image formation. The light captured by the objective is spread over a small spot also known as the Airy disc, with diameter d_{diff} , surrounded by diffraction rings of decreasing brightness. The size of the image can be regulated by varying the value of $f/\#$ which controls the aperture diameter (see eq(4.8)) of the camera. The $f/\#$ is generally adjusted to a value such that the image of the particles occupy 2-3 pixels in the image (see (4.1.5) for details). In practice, for PIV images, the light distribution in the Airy disc is well approximated by a Gaussian intensity distribution.



(a) Airy diffraction pattern



(b) Airy function approximated by a Gaussian

Figure 4.4: Normalized intensity distribution of the Airy pattern and its approximation by a Gaussian bell curve.

4.1.5 Digital Image Recording

The image plane of the camera coincides with a sensor constituted of a 2-D array of pixels. The light exposed to the sensor is digitally converted, for each pixel, into an intensity level on a gray scale. The optical and electronic mechanical characteristics of the sensors have a direct influence on the image acquisition rate and the errors connected to it. A major source of this noise is due to thermal effects which also generate electron-hole pairs that cannot be separated from those generated by the photoelectric effect. Another source of noise is read noise or shot noise which is a direct consequence of the charge-to-voltage conversion during the readout sequence. In general, the read noise increases with the readout frequency which is why many scientific applications require slow-scan cameras which limits the frequency of acquisition.

CCD sensor or Charge Couple Device is an electronic sensor that converts light (photons) into free electrons. When discharged, current and voltage proportional to the charge accumulated are produced. Two-dimensional array sensors for imaging are obtained placing the

individual sensitive elements (pixels) on a Cartesian grid. Modern CCDs have a typical size of several mega-pixels.

CMOS sensors are based on active pixel sensor (APS) technology: each pixel is an isolated circuit and, in addition to the photo diode, can be provided with a local amplifier. After the integration period the photo-electric charge is transferred through a row selector to a row bus and further amplified; the process is repeated for each row until covering the whole image. CMOS sensors allow higher image contrast with respect to CCD and eliminate blooming(electrons migration from overcharged pixel to the neighboring pixels)and have emerged as an alternative to charge-coupled device (CCD) imager sensors. Although CMOS sensors allow for a non-linear amplification and conversion of the signals on chip, linear amplification is preferred in PIV.

f-stop and imaging: The typical size of CCD pixels is of the order of $10\mu m$. Consider two possible situations for particle image size as shown in the figure below : $d_\tau < 1$ pixel and $d_\tau \simeq 3$ pixels. The second case is more favorable for PIV because the position of the particle images

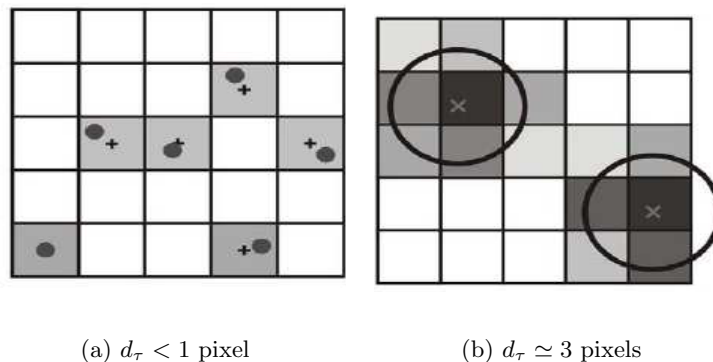
(a) $d_\tau < 1$ pixel(b) $d_\tau \simeq 3$ pixels

Figure 4.5: Digital imaging of small particles

can be reconstructed from the interpolation of the light intensity distribution spanning several pixels. In the first case, the particle position altogether with its light distribution information is irreversibly lost and is said to be optically under sampled. However if the particle images become too large the situation deteriorates again because the individual particle images would start to mutually overlap decreasing the image contrast and the spatial resolution of the measurement. The optimum situation is a compromise between the above requirements and is obtained when $d_\tau = 2 - 2.5$ pixels.

As mentioned in the previous section, $f/\# = f/D$ is generally adjusted to a value such that the image of the particles occupy $2 - 3$ pixels in the image[see eq (4.8)]. Since the focal length(f) of the camera is a constant, the $f/\#$ is adjusted by varying the aperture diameter(D).

Camera shuttering time has to be synchronized with the time interval between the laser pulses such that each camera exposure corresponds to only one laser pulse. A sketch of this

so called frame straddling mode for Double Frame/Single Exposure acquisition used for the present experiment is drawn in Figure (4.6) T_{shut} is the camera shutting time for data transfer, δt is the laser pulse separation which governs the time interval between the image pairs and ΔT is the time interval between the two acquisitions which governs the acquisition frequency of TR-PIV. Note that the acquisition frequency is half the recording rate of camera.

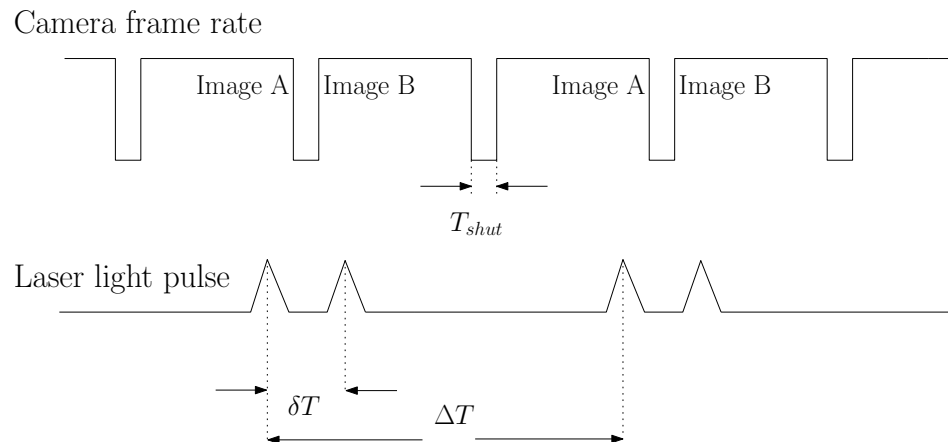


Figure 4.6: Timing diagram based on Double Frame/Single Exposure frame straddling mode

4.2 Digital PIV Evaluation

In the following we describe the necessary steps in the fully digital analysis of PIV recordings using statistical methods. The basic operations needed to evaluate the motion field of the particle tracers is schemetized in fig(4.7):

1. **Image windowing:** the entire imaged is partitioned into small cells each of them containing a statistically significant number of tracers($\simeq 8$). In practice, the *one-quarter rule* is the factor used for smallest window-size. Every interrogation cell or window becomes an individual measurement volume where the local velocity vector is evaluated.
2. **Cross-correlation analysis:** a statistical tracking operator is applied to the corresponding windows extracted from the two exposures. This process returns the discrete cross-correlation map (a two dimensional array), in which the peak position relative to the origin indicates the average particle images displacement
3. **Correlated peak sub-pixel interpolation:** the highest peak in the correlation map is selected as that corresponding to the particle motion. Its position is naturally found at the closest integer pixel shift. A more accurate peak position estimate requires the interpolation of the peak.
4. **Divide by time and scaling:** the result obtained at point (3) yields the particle motion in terms of pixel shift between the corresponding windows. The velocity is obtained dividing by the known time separation between laser pulses, multiplying by the size of the pixel and dividing by the imaging magnification.

The discrete cross correlation function R reads as

$$R_{II}(m, n) = \sum_{i=-K}^{K} \sum_{j=-L}^{L} [I(m, n)][(I'(i + m, j + n)] \quad (4.9)$$

where,

I and I' indicate the light intensity distribution on the pixels in the interrogation window at time t and $t + \Delta t$ respectively. Essentially the template I is linearly shifted around in

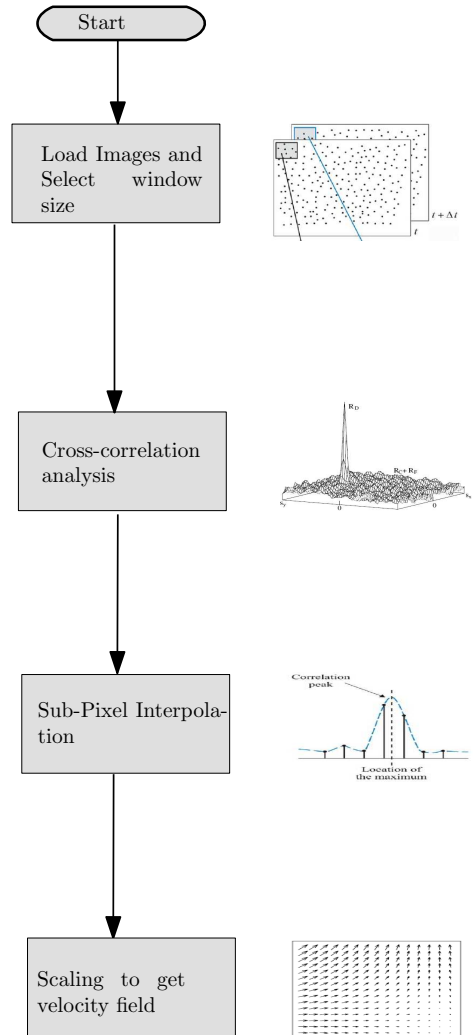


Figure 4.7: Block diagram of the Digital PIV Evaluation

the sample I' without extending over edges of I' . For each choice of sample shift (m, n) , the sum of the products of all overlapping pixel intensities produces one cross-correlation value $R_{II}(m, n)$. By applying this operation for a range of shifts $(-K \leq i \leq +K, -L \leq j \leq +L)$, a correlation plane the size of $(2K + 1) \times (2L + 1)$ is formed.

4.2.1 Frequency domain based correlation

In practice, Cross correlations are usually implemented using fast-fourier transforms, according to convolution theorem.

$$R_{II} \iff \hat{I} \cdot \hat{I}' \quad (4.10)$$

where, \hat{I} and \hat{I}' are the Fourier transforms of the functions I and I' , respectively. The advantage of Frequency domain based correlation is drastic reduction in computation time and memory requirement. The computational efficiency can be increased even further by observing the symmetry properties between real valued functions and their Fourier transform, namely the real part of the transform is symmetric: $Re(\hat{I}_i) = Re(\hat{I}_{-i})$, while the imaginary part is antisymmetric: $Im(\hat{I}_i) = -Im(\hat{I}_{-i})$. which reduces the computations from $O[N^4]$ operations to $O[N^2 \log_2 N]$ operations.

However, use of two-dimensional FFTs for the computation of the cross-correlation plane has a number of properties whose effects have to be dealt with. The use of symmetry property requires the input data to have a base-2 dimension (i.e. 32×32 pixel or 64×64 pixel samples). Periodicity of data is assumed during the evaluation of Fourier Transform causing measurements to be aliased and introduction of bias errors.

4.3 Limitations of Digital PIV Evaluation

- The velocity dynamic range is limited due to the conflict between the interrogation window size and the in-plane displacement that causes loss of pairs.
- A velocity bias (systematic underestimation) occurs, due to the finite extent of the interrogation window, resulting into a trade-off between accuracy and spatial resolution.
- The fractional displacement estimate is dependent on the peak interpolation function. A typical form of error introduces a bias towards integer values of the displacement bringing the measurement accuracy back to its discrete nature. The phenomenon is thus referred to as peak locking.
- Peak locking error also occurs when the particles images are sampled at a poor spatial resolution (particle image size smaller than two pixels).
- The correlation peak signal drops in regions with a large velocity gradient. Loss of pairs is due to the particle image pattern deformation.
- The spatial resolution of the method is limited by the minimum number of particles in the interrogation window.

4.4 Advanced Digital Interrogation Techniques

4.4.1 Image normalisation

The digital images are pre-processed using a normalization software to remove the reflections from the edges of cavity and extraneous noise from the digital image using a matlab code. Since the images of particles are transient at a particular location in the field of view, the time average of images will have contribution only from the reflections which does not change in time. The images are divided by its time average to reduce the effect of reflections. Each image is also normalised by its spatial average.

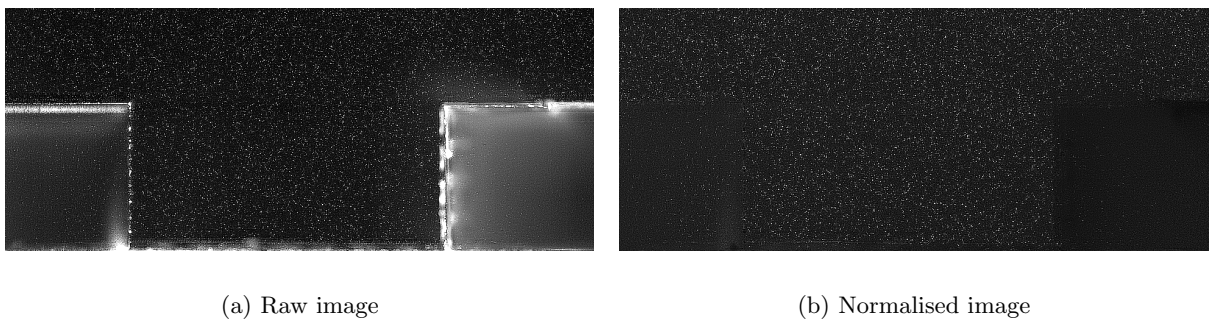


Figure 4.8: Normalisation of raw images before cross-correlation

4.4.2 Window Off-Setting

In this technique, the interrogation windows are off-set according to the mean displacement (estimated usually by an iteration scheme) so that the fraction of matched particle images to unmatched particle images is increased. This technique not only increases the signal-to-noise ratio of the correlation peak, but also increases the accuracy of velocity estimation when the displacements are less than half a pixel. The interrogation window offset can be relatively easily implemented in an existing digital interrogation.

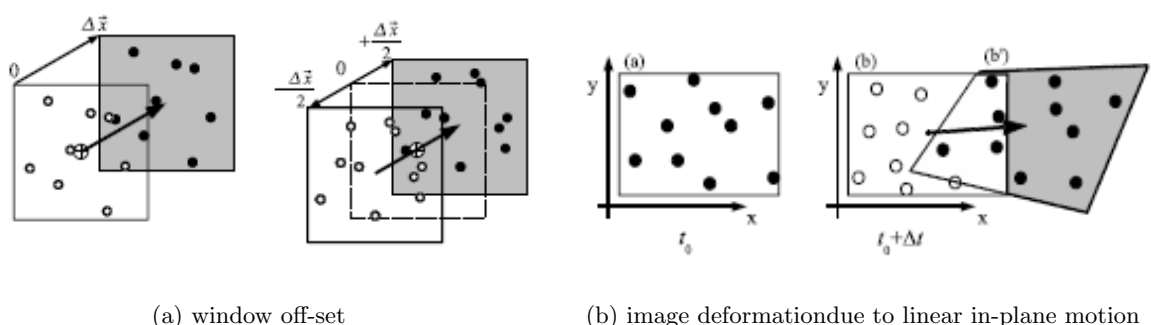


Figure 4.9: Window Off-Setting and Window Deformation

4.4.3 Window Deformation

Window off-set technique fails to resolve the large velocity gradients (turbulent flow, shear flow) where velocity field exhibits significant variations within the interrogation window. This limitation is overcome by Window Deformation technique every location in the image is deformed based on the velocity-field predictor (estimated by an iteration scheme) using an interpolation.

4.5 Window Deformation Iterative Multigrid Algorithm

PIV processing in the present work has been performed using the MATLAB software WIDIM (Window Deformation Iterative Multigrid) developed by [Scarano and Riethmuller \(1999\)](#) and updated at the TU Delft.

The two main feature of this algorithm are

1. Multi-grid analysis
2. Iterative analysis with Image Deformation

Multi-Grid Analysis: The interrogation window size is progressively decreased. The velocity field obtained at each level is used as first the predictor for the iterative analysis of the next level. This process eliminates the *one-quarter rule* constraint and user has the freedom to use smaller windows and thus obtain better resolution.

Iterative Analysis with Image Deformation: An iterative analysis is performed on the image pairs at fixed window size (at every level of multi-grid analysis). This process allows to further improve the accuracy of the image deformation ([Scarano and Riethmuller \(1999\)](#)) and to a certain extent allows to enhance the spatial resolution of the measurement. In its essence the process can be described by a predictor-corrector loop as described below.

At each iteration level, k the image-pair is deformed from the original image-pairs based on the velocity prediction, \mathbf{V}^k obtained from previous iteration. The image deformation displacement at every location in the image is obtained by interpolating the predictor displacement \mathbf{V}^k onto a pixel grid using `sinc` interpolation with an 11×11 pixel kernel size. The correction displacement \mathbf{C}^k determined by cross-correlation of the deformed image-pair is then used to predict the deformation in the next iteration level.

$$\mathbf{V}^{k+1} = \mathbf{V}^k + \mathbf{C}^k \quad (4.11)$$

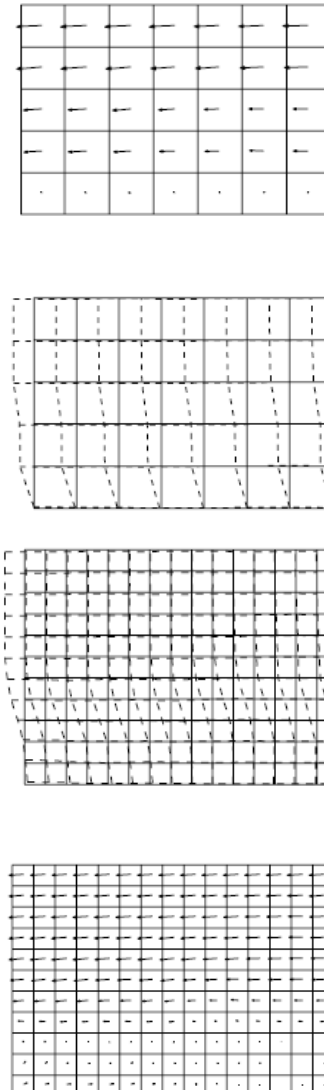


Figure 4.10: Window Deformation in Iteration Loop

The interpolation schemes together with iteration loop can introduce fluctuations in velocity estimation. This is stabilized using spatial filtering of predictor and corrector.

4.6 Time Resolved-PIV

Temporally Resolved Particle Image Velocimetry (TR-PIV) is a powerful tool developed in recent years to support our continuing efforts to characterize and improve our understanding of transient turbulent flow a critical element for understanding the acoustic properties of turbulent flows. The rapid advancement in high speed digital cameras and Laser technology has made TR-PIV system capable of acquiring planar PIV image frame pairs at very high frequencies at high spatial resolution. FASTCAM SA1.1 cameras are capable of over 5400 frames per second(fps) of ($1K \times 1K$) mega pixels format. The new CMOS sensors provide twelve bit pixel depth.

Chapter 5

Planar pressure imaging

5.1 Introduction

Wall pressure fluctuations are responsible for excitation of structures, leading to flow-induced vibrations and noise. Pressure is also a dominant contributor to the lift and form drag for a body moving in fluid. Knowledge of the pressure distribution in a flow field is thus a primary concern in many engineering applications. The instantaneous velocity and acceleration fields are acquired by TR-PIV to estimate instantaneous pressure fields using the in-plane pressure gradient components. This non-intrusive measurement method provides a high spatial and temporal resolution which is unavailable when using pressure transducers. The following chapter offers an overview of the methodologies used in evaluating pressure from PIV vector fields.

5.2 Mathematical formulation

Navier-Stokes Equation in differential form can be rearranged to get pressure gradient:

$$\nabla p = -\rho \cdot \left(\frac{D\mathbf{V}}{Dt} - \nu \nabla^2 \mathbf{V} \right) \quad \text{Navier - Stokes Equation} \quad (5.1)$$

On the other hand Poisson Equation for Pressure could also be obtained by taking divergence on both sides of above equation (5.1)

$$\nabla^2 p = -\rho \nabla \cdot \left\{ \frac{D\mathbf{V}}{Dt} + \nu \nabla^2 \mathbf{V} \right\} \quad \text{Poisson Equation} \quad (5.2)$$

where, $\frac{D\mathbf{V}}{Dt}$ is the material acceleration given by

$$\frac{D\mathbf{V}}{Dt} = \partial \mathbf{V} / \partial t + \mathbf{V} \cdot \nabla \mathbf{V} \quad (5.3)$$

and $(\nu \nabla^2 \mathbf{V})$ is the viscous term

5.2.1 Acceleration

Acceleration fields, $D\mathbf{V}/Dt(x, y, t)$ are computed from instantaneous velocity fields, $(\mathbf{V}(x, y, t))$, acquired by TR-PIV. Although, 2-D description of the flow field obtained from TR-PIV is incomplete, [Haigermoser \(2009\)](#) pointed out that pressure is a scalar and can be integrated in a plane without requiring the normal pressure gradients. The projection of the material acceleration onto a 2-D plane is an approximation that is valid in a 2-D flow.

5.2.2 Viscous terms

In a high Reynolds number flow field located away from boundaries, the material acceleration is dominant and the viscous term ($\nu \nabla^2 \mathbf{V}$) is negligible. As shown by [Liu and Katz \(2006\)](#), experimental data for a cavity shear flow indeed confirms that the material acceleration is the dominant term. However, one should be careful to evaluate the contribution of the viscous term and avoid integrating along paths that are particularly affected by viscosity, e.g., along a boundary layer.

5.2.3 Boundary conditions

[Gresho and Sani \(1987\)](#) have pointed out that the physical boundary conditions are to be derived from the conservation of momentum, namely the Navier Stokes equations. The correct boundary conditions for incompressible flow are, therefore, the Neumann boundary conditions rather than the Dirchelet conditions although they showed that Dirichlet and Neumann boundary conditions for the pressure Poisson equation give the same solution. [Abdallah and Dreyer \(1988\)](#) confirmed this (for one case at least) by numerically solving the pressure equation with Dirichlet and Neumann boundary conditions for the inviscid stagnation point flow problem. The Dirichlet boundary condition is obtained by integrating the tangential component of the momentum equation along the boundary. The Neumann boundary condition is obtained by applying the normal component of the momentum equation at the boundary. Particle Image Velocimetry can be used to provide the required boundary pressure conditions by applying the Navier Stokes equations on the boundary.

5.3 Classification of PPI methods

Based on the way accelerations are evaluated PPI technique may be categorized into:

1. Eulerian Approach
2. Lagrangian Approach

Basically two strategies have been proposed in literature for Planar Pressure Imaging:

1. Direct Spatial Integration
2. Planar Poisson Formulation

5.3.1 Planar poisson formulation using Eulerian approach

Gurka et al. (1999) made the first attempt to use PIV data to solve the Poisson Pressure Equation(5.2) for *incompressible steady non-viscous flow (and mean turbulent flow)*. Therefore, the time derivative, $\partial V/\partial t$ and viscous, $\nu\nabla^2V$ terms were zero and the PIV data was used to compute the $p\{V \cdot \nabla V\}$. The Poisson equation is reduced to

$$\frac{\partial^2 p}{\partial x^2} + \frac{\partial^2 p}{\partial y^2} = -\rho \left\{ \left(\frac{\partial u}{\partial x} \right)^2 + \frac{\partial v}{\partial x} \frac{\partial u}{\partial y} + \left(\frac{\partial v}{\partial y} \right)^2 \right\} \quad (5.4)$$

The pressure fields are computed in combination with the instantaneous velocity data under Neumann boundary conditions by solving the Poisson equation numerically using the Liebmann successive over relaxation(SOR) iteration scheme. Two types of pressure averaging were obtained. The Poisson equation (5.2) was used to compute the instantaneous pressure for each instantaneous velocity realization and then averaged. Alternatively, the mean pressure was computed directly using the turbulent Poisson equation.

$$\nabla^2 p = -\rho\{\mathbf{V} \cdot \nabla \mathbf{V}\} + \nabla \cdot \partial/\partial x_j (\bar{u}_i' u_j') \quad (5.5)$$

N. Fujisawa and Srinivas (2005) evaluated pressure field and fluid forces on a circular cylinder in a uniform flow ($Re = 2000$) using the same pressure Poisson equation (5.2) in combination with the instantaneous velocity data obtained from PIV. They concluded the validity of the PPI technique by observing close agreement between their results and literature. Although, they claim to have evaluated “instantaneous pressure fields” around oscillating cylinder, they neglected the $\partial/\partial t$ terms (along with out-of-plane gradients) in Poisson equation (5.2).

5.3.2 Direct spatial integration using Eulerian approach

In the direct approach the pressure gradients are integrated directly from reference points (Dirichlet boundary condition) using a spatial marching erosion scheme which introduces a dependence on its integration path.

Eulerian form of the Navier-Stokes-equations can be obtained by substituting (5.3) in (5.1)

$$\nabla p = -\rho\{\partial \mathbf{V}/\partial t + \mathbf{V} \cdot \nabla \mathbf{V} - \nu \nabla^2 \mathbf{V}\} \quad (5.6)$$

Baur and Kongeter (1999) further simplified the above equation for two dimensional case applied the continuity and incompressibility condition to evaluate the out-of-plane gradient $\partial w/\partial z$. The pressure gradient Δp finally integrated along the grid points (the explicit integration scheme is indicated in Fig(5.1)). For each grid point the already calculated neighbor grid points are used as integration paths. The pressure in the investigated grid point is determined as the mean of the so estimated values in order to reduce the effect of uncertainties in the measurements:

$$p = \frac{1}{4} [(p_1 + \Delta p_1) + (p_2 + \Delta p_2) + (p_3 + \Delta p_3) + (p_4 + \Delta p_4)] \quad (5.7)$$

Roeland de Kat et al. computed the pressure field around a stationary square section cylinder using two different strategies (both employed the eulerian approach):

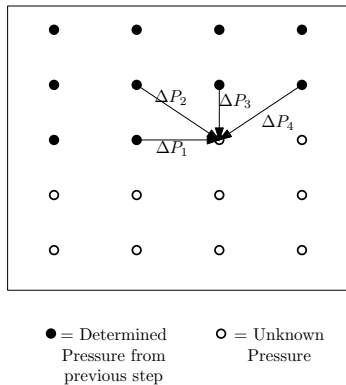


Figure 5.1: Schematic of pressure integration paths by Baur and Kongeter

1. Direct spatial integration
2. Planar poisson formulation

He found satisfactory results from computation of the pressure fields. He concluded that large scale pressure fluctuations and mean pressure are captured correctly by both PPI strategies and they agree well with pressure orifice, microphone. However, a detailed uncertainty analysis of determining the pressure and pressure gradient with PPI(where the out-of-plane gradients and temporal gradients, $\partial/\partial t$, are neglected in Poisson Equation) still need to be performed.

5.3.3 Direct spatial integration using Lagrangian approach

Liu and Katz (2006) used four-exposure PIV to obtain velocity fields, and used “pseudo-tracing” technique to measure the Lagrangian acceleration $D\mathbf{V}/Dt$ of the flow, and by integration of Navier-Stokes equation in Lagrangian form (5.1), obtained the pressure distribution for a 2D cavity flow field. An omni-directional virtual boundary integration scheme was used to integrate the spatial distribution of acceleration. Multi-integration paths minimize the effect of local random errors in acceleration. Further improvements were achieved by iterations to correct the pressure along the boundary. They claimed that their Direct Method gave more accurate results than Poisson approach, which involves second derivatives of the measured velocity (resulting in large errors) making it suitable only for laminar flow or time averaged pressure distribution of planar turbulent flow.

5.3.4 Planar poisson formulation with Lagrangian approach

Moore, proceeded in the same lines as Liu and Katz (2006) but used an interpolation between the velocity fields obtained from TR-PIV data for higher order approximation of pathlines over which the Lagrangian accelerations $D\mathbf{V}/Dt$ can be computed. The pressure was evaluated from Poisson Solver provided by Roeland de Kat et al.. The chief advantage of Lagrangian approach, as pointed out my Moore, is that the time resolution of the PIV system is sufficient to capture the development of flow features, in a reference frame that is moving with those features. However, it is not sufficient to capture the point-wise instantaneous changes of an Eulerian perspective.

This strategy was employed in computation of pressure for the present case : Cavity Flow.

5.4 Planar pressure imaging of cavity flow

At high Reynolds number and low mach number the flow can be considered non-viscous and incompressible. The poisson equation under these assumptions reduces to

$$\nabla^2 p = -\rho \nabla \cdot \left\{ \frac{D\mathbf{V}}{Dt} \right\} \quad \text{Poisson Equation} \quad (5.8)$$

The pressure is computed from the 2D velocity fields using a pressure solver based on Planar Poisson Formulation with Lagrangian Approach. The PPI solver used in this project is developed by Peter Moore. The viscous stress terms are ignored and out of plane velocity gradients are not considered. The solver uses an interpolation between the velocity fields, for higher order approximation of pathlines over which the Lagrangian accelerations, $\frac{D\mathbf{V}}{Dt}$ are computed. The pressure is evaluated from Poisson Solver provided by [Roeland de Kat et al.](#).

Neumann boundary conditions are applied at the boundaries of the domain:

$$\nabla p = -\rho \left\{ \frac{D\mathbf{V}}{Dt} \right\} \quad \text{Neumann}$$

Dirichlet boundary condition is applied at the upper limit of the domain :

$$p = \frac{1}{2} \rho (U_\infty - \mathbf{V}^2) \quad \text{Dirichlet}$$

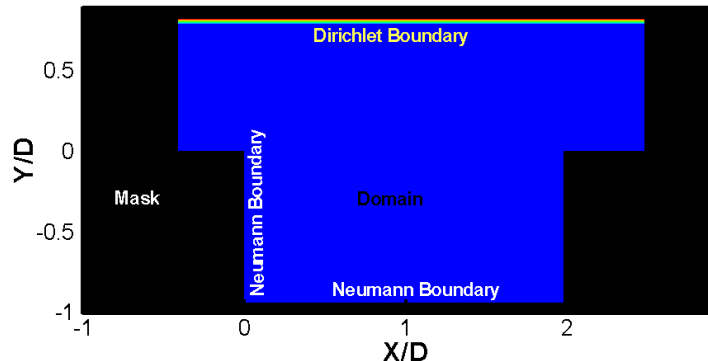


Figure 5.2: Domain and Boundaries for pressure computation using PPI

Chapter 6

Experimental Investigation

6.1 Experimental facility

The experiments were carried out at Vertical Low Turbulence Tunnel, an open jet wind tunnel of the Aerodynamics Laboratories at the TU Delft. The inflow is through a circular exit with a diameter of 0.6m diameter. Due to the high contraction ratio of the settling chamber the quality of the airflow is very high in terms of the turbulence level that is smaller than 0.1%. Also, tunnel is relatively silent, which enables performing aeroacoustic experiments. The maximum achievable velocity is 45m/s.

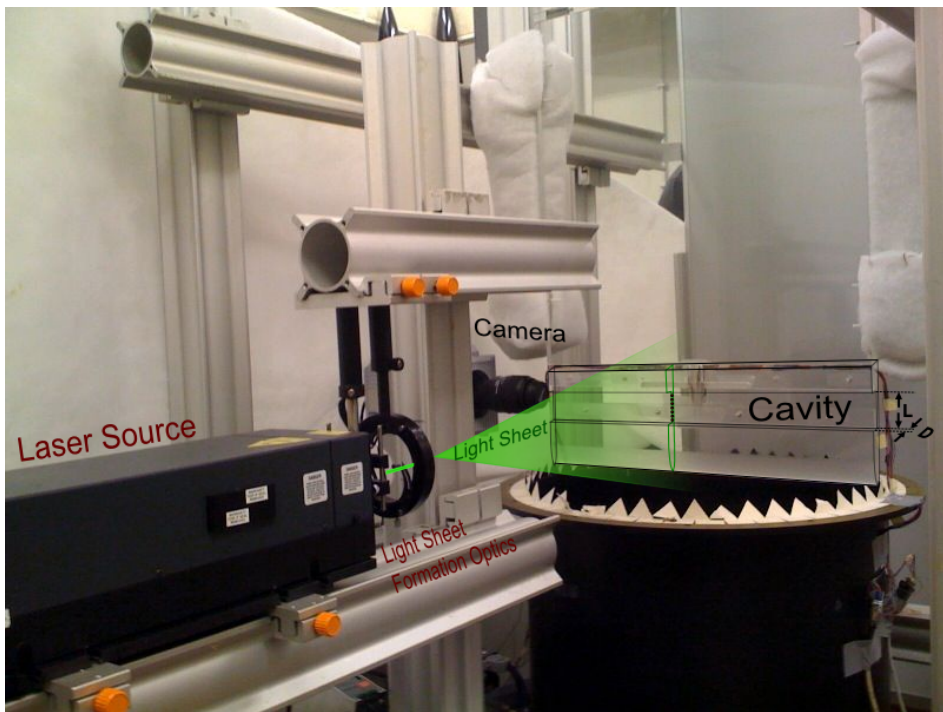


Figure 6.1: Experimental Facility

6.2 Experimental Set-up

The test model, as shown in the figure, is a flat plate made of transparent plexi-glass 85 cm long and 60 cm wide and 2.5 cm thick with an elliptical nose(major axis= 6 cm ,minor axis=2.5 cm). The rectangular cavity of length, $L = 3$ cm and depth, $D = 1.5$ cm is located 120 cm behind the nose. The elliptical nose as the leading edge in the flow provides a smooth and steady attached flow ahead of the cavity. Microphones numbered $M1$ through $M11$ are placed on the walls of the cavity at locations shown in the figure below and microphones $M12-M15$ were located in the acoustic field 47cm from the lip of the cavity. All microphones used were high-sensitivity and high-frequency Sonion 800 series pressure transducers which acquired data at 100,000 Hz.

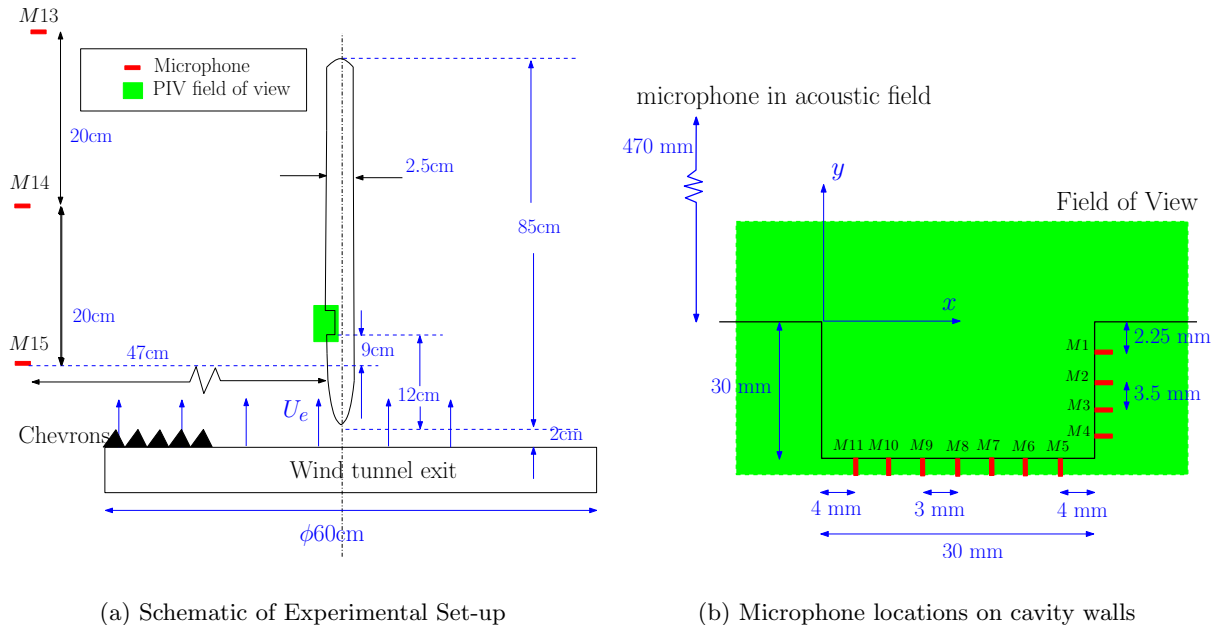


Figure 6.2: Experimental Set up

Figure 6.2 shows the the schematic of test configuration. The nose of the test-model is 2 cm from the circular exit of the wind tunnel. To minimize possible acoustic reflections from the rail system, the laser box and laser generator were covered in absorbing foam. Chevrons were placed around the wind-tunnel exit perimeter to minimise noise from the shear layer generated at the exit.

Two-component time-resolved particle image velocimetry (2C-TR-PIV) was used to obtain planar velocity field measurements around the rectangular cavity. Safex stage smoke generator was used to seed the flow with particles of approximately $1\text{ }\mu\text{m}$ diameter. The seeding was introduced at the inlet of the wind tunnel system, which provided a homogeneously seeded flow at the test section. The particles were illuminated by laser light sheet(527 nm wavelength) produced by Pegasus-PIV, a dual-head, high repetition rate, diode-pumped Nd:YLF laser system. The plane of light sheet was placed at the mid-span section of the test model. Photron Fast CAM SA1 CMOS camera was used for the image acquisition. The camera was

equipped with a Nikon objective with a focal length $f = 0.105$ m in order to capture the required field of view of $60\text{ mm}^2 \times 30\text{mm}^2$ on an digital image (1024×512 pixels). Numerical aperture was set to $f/\# = 5.6$ to obtain required size of particle image.

The experiments were conducted at three different free-stream velocities ($U_e = 10, 12, 15$ m/s) with both laminar and turbulent incoming flow conditions. The turbulence was generated using a cylindrical trip wire placed before the cavity.

The experimental investigation described above can be summarised in the table below.

TR-PIV									
Parameters									
Flow	Free-stream velocity(U_e)	10m/s	12m/s	15m/s					
	Mach number (M)	0.029	0.035	0.044					
	Reynolds number (Re)	1.9×10^4	2.3×10^4	2.8×10^4					
	Incoming flow	Laminar	Laminar	Laminar	Turbulent				
Seeding	Seeding Source	Safex stage smoke generator							
	Particle diameter	$1\mu\text{ m}$							
Illumination	Laser source	Pegasus-PIV							
	Laser type	diode-pumped Nd:YLF, dual head							
	Laser pulse separation								
Imaging	Camera	Photron Fast CAM SA1 CMOS							
	focal length (f)	0.105							
	Numerical aperture($f/\#$)	5.6							
Recording	Recording Method	double frame/single exposure							
	Image size	1024×512 pixels							
	Field of view	$60\text{ mm}^2 \times 30\text{mm}^2$							
	Pixel size	17mm							
	Frequency of acquisition	3125 Hz							
Microphones									
Microphone	Sonion 8000 series								
	Type	Condensor							
	Sampling Frequency	100KHz							

Table 6.1: Experimental Parameters

6.3 Data reduction techniques

Two successive normalized images obtained from 2D-TR-PIV were cross-correlated to obtain the velocity fields using WIDIM (Window Deformation Iterative Multigrid) algorithm (see section(4.5) for details) with an initial interrogation window size of 121×121 pixels and a final interrogation window size of 31×31 pixels with a 75% overlap, applying sub-pixel refinement and window deformation. Hence, one vector corresponds to the velocity in a spatial area of 0.47×0.47 mm 2 . The pressure is computed from the 2D velocity fields using a pressure solver based on Planar Poisson Formulation with Lagrangian Approach. The Acoustic Analogies were then implemented using the pressure data to compute the sound in acoustic field.

Chapter 7

Results and Discussions

In this chapter the results of PIV post-processing, planar pressure imaging and implementation of acoustic analogies will be discussed. First, cavity flow physics is discussed where mean flow quantities and instantaneous quantities are presented. The pressure fields obtained from PPI are then discussed and an attempt is made to relate the flow dynamics to the pressure fluctuations in the cavity flow. The pressure computed from PIV-PPI is compared with the microphones on the walls of the cavity. Next, the acoustic analysis of the cavity is presented. Curle's analogy and Gutin's principle was implemented to compute sound in the acoustic field of the cavity. Finally, comparison between acoustic data obtained from microphone measurements and acoustic analogy are presented.

7.1 Cavity Flow Physics

7.1.1 Time averaged flow features

The time averaged flow properties were obtained from an ensemble of 700 velocity fields. The figure (7.1) shows the contour plots of stream-wise velocity, vertical velocity and standard deviation of stream-wise and vertical velocity components respectively. All the mean quantities are normalised with the free-stream velocity (U_e) and are plotted in Figure (7.1). Contour plot of stream-wise velocity in Figure 7.1(a) clearly indicates presence of a shear layer spanning the mouth of cavity.

The shear layer is formed when the laminar incoming flow arrives at the upstream edge, generating a mixing layer with the no-flow fluid inside the cavity. This phenomenon, called Kelvin-Helmholtz instability grows in size until the mean velocity profile experiences an inflectional point which is unstable. The saturation of the primary instability leads to nonlinear two-dimensional rolls, referred to as Kelvin-Helmholtz vortices.

Figure(7.1(c) and 7.1(d)) show large fluctuations in velocity after the inflectional point, indicating presence of vortex shedding in the region.

The shear layer drives a circulation region inside the cavity. In fact, the streamlines of the mean velocity field (Figure 7.1(b)) show presence of two circulation zones: a large recirculation zone in the downstream part of the cavity and also a smaller one in the upstream part.

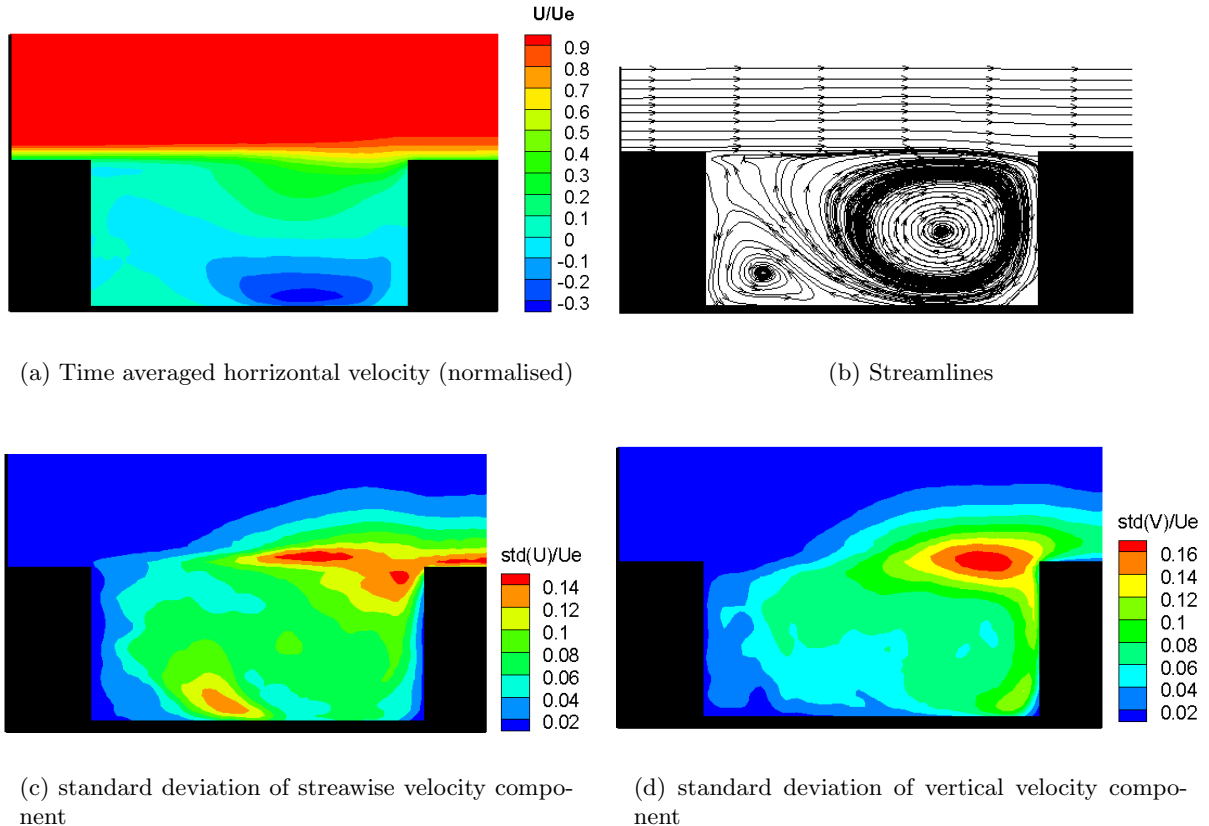


Figure 7.1: Mean quantities in the flow at $U_e = 10\text{m/s}$, laminar incoming boundary layer

7.1.2 Unsteady flow

A sample of five snapshots over one vortex shedding period of the cavity flow is shown in Figure (7.2), where the color levels represent the magnitude of the velocity components normalised with free stream velocity(U_e). The vortex core convecting in the shear layer can be visualized from the closely spaced patches of positive and negative velocities(v/U_e). The ratio of convective velocity of vortices and free stream velocity, as deduced from the contour plots of stream-wise velocity component, is $u/U_e = 0.6$. This is very close to the empirical value of γ which Rossiter used in the acoustic feed-back mechanism (see equation(2.1)).

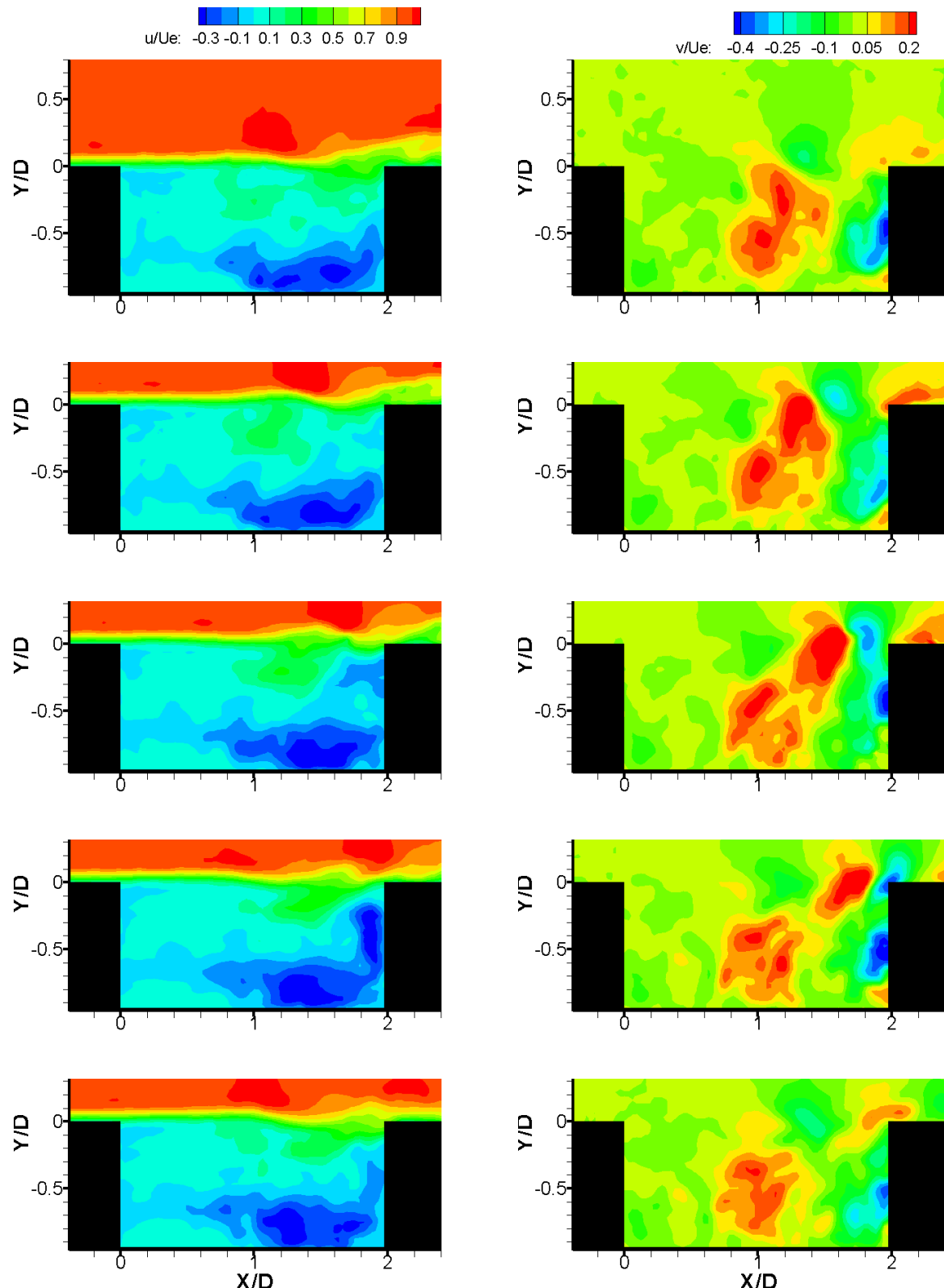


Figure 7.2: Instantaneous velocity fields in a shedding period for mean flow = 10m/s
MSc. Thesis

: streamwise(left) and vertical(right)

D.Parkhi

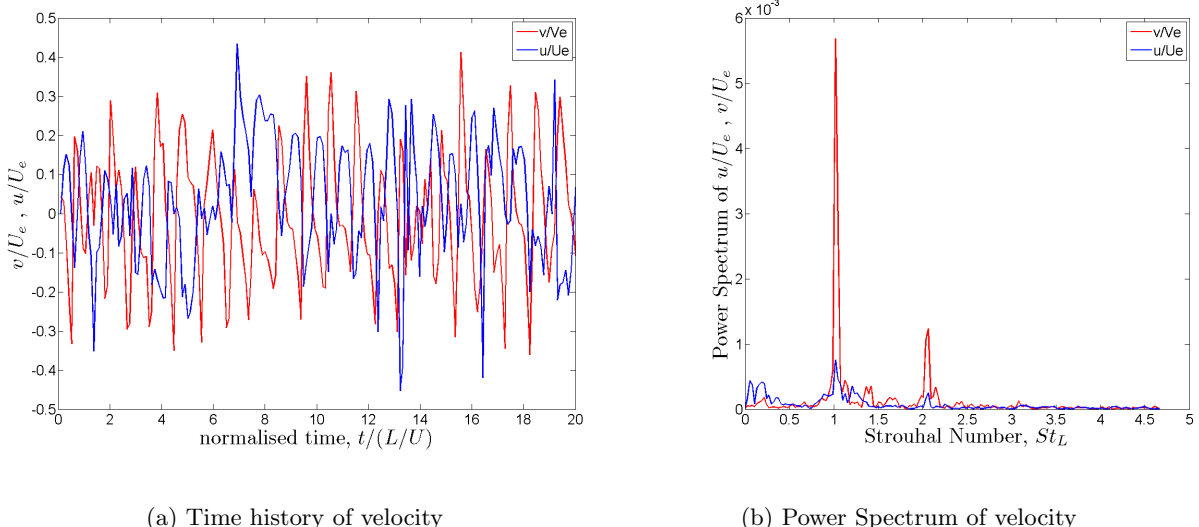


Figure 7.3: Time history and Power Spectrum of velocities near the trailing edge of cavity: $X = 0.9L$, $Y = 0$ at $U_e = 10\text{m/s}$

The periodic shedding of vortex can be analysed from the time history of velocity fluctuations near the trailing edge of the cavity form the PIV data. Figure (7.4(a)) shows the time history of stream-wise component and horizontal component of velocities near the trailing edge of the cavity($X = 0.9L$, $Y = 0$) when the free-stream velocity, $U_e = 10\text{m/s}$. Figure (7.3) shows the power spectrum of the velocities. A clear peak is visible at a Strouhal number based on the cavity length L, $St_L = 1.02$. Similar analysis was performed for all the three mean stream velocities $U_e = 10, 12, 15$ and tonal frequencies were compared to Rossiter's prediction.

Free Stream Velocity, U_e (m/s)	Tonal Frequencies (St_L)		
	Rossiter Equation	PIV	
	$m = 1$	Peak 1	Peak 2
10	0.98	1.02	2.06
12	0.98	1.14	2.28
15	0.97	1.1	2.2

Table 7.1: Tonal Frequencies and Rossiter Modes at $U_e = 10, 12, 15$ m/s

Table (7.1) lists the Strouhal numbers corresponding to the rossiter modes and the Strouhal number corresponding to the tonal peaks observed in the flows at $U_e = 10, 12, 15$ m/s. The observed Strouhal numbers correspond to the first peak, are close to the vortex shedding frequency of the second Rossiter mode ($St_{L_m=1}$). A small peak at twice the Strouhal number of primary peak shows that the second harmonics are also resolved by the spectral analysis of PIV data.

7.1.3 Pressure fluctuations

Instantaneous pressure fields computed using PPI techniques (described in Chapter 5) are shown in Figure (7.5) along with the vorticity field computed from PIV analysis over one vortex shedding period. The shear layer spanning from the leading edge of the cavity is stable till about $x/D = 1$ where the vortices seem to start shedding. This is the inflectional point as described before. The vortices are convected down stream and impinge on the trailing edge of the cavity producing noise. The frequency of vortex arrival at the trailing edge corresponds to Stouhal number $St_L = 1$.

It was also observed that the location of this inflectional point moves up-stream as the mean-stream velocity increases. This is because the incoming boundary layer is thinner for higher velocity and its ability to withstand the velocity gradient across the shear layer reduces and hence starts shedding vortex at an early stage.

It can also be easily observed from the visual inspection of corresponding pressure fields that pressure fluctuations are directly correlated with the vortex shedding.

Figure (7.4) shows the power spectrum of the vertical velocity, v (normalized with free-stream velocity) and pressure, p (normalised with dynamic pressure $0.5 \rho U_e^2$) at $y/D = 0$; $x/L = 0.95$.

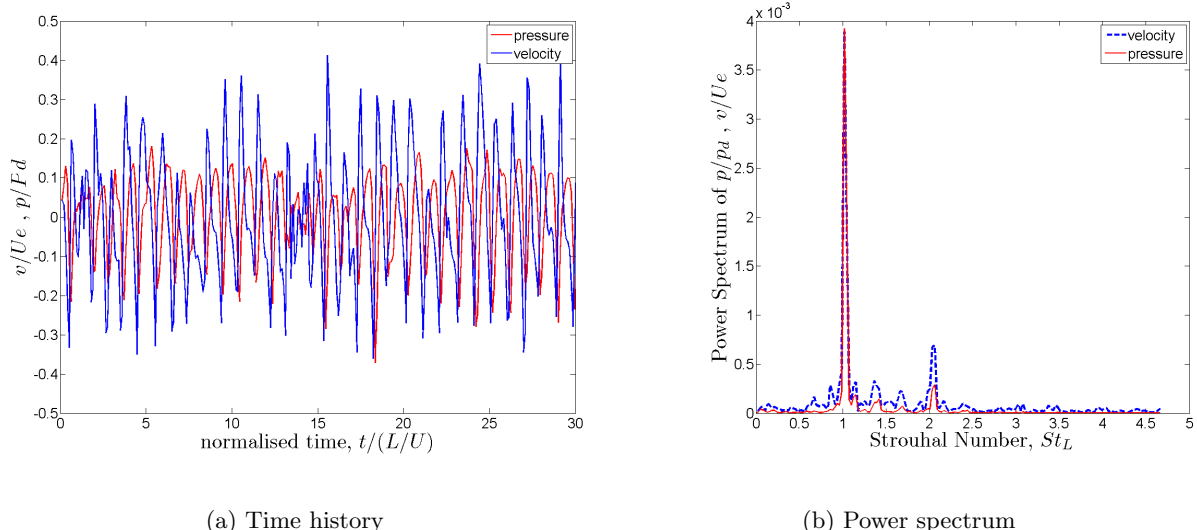


Figure 7.4: Velocity and Pressure at $y/D = 0$; $x/L = 0.95$ for $U_e = 10$ m/s

The spectrum of the pressure coefficient and normalised velocity calculated at the same location reveals again a peak at same Strouhal numbers, which confirms that the pressure fluctuations are related to the vortex shedding.

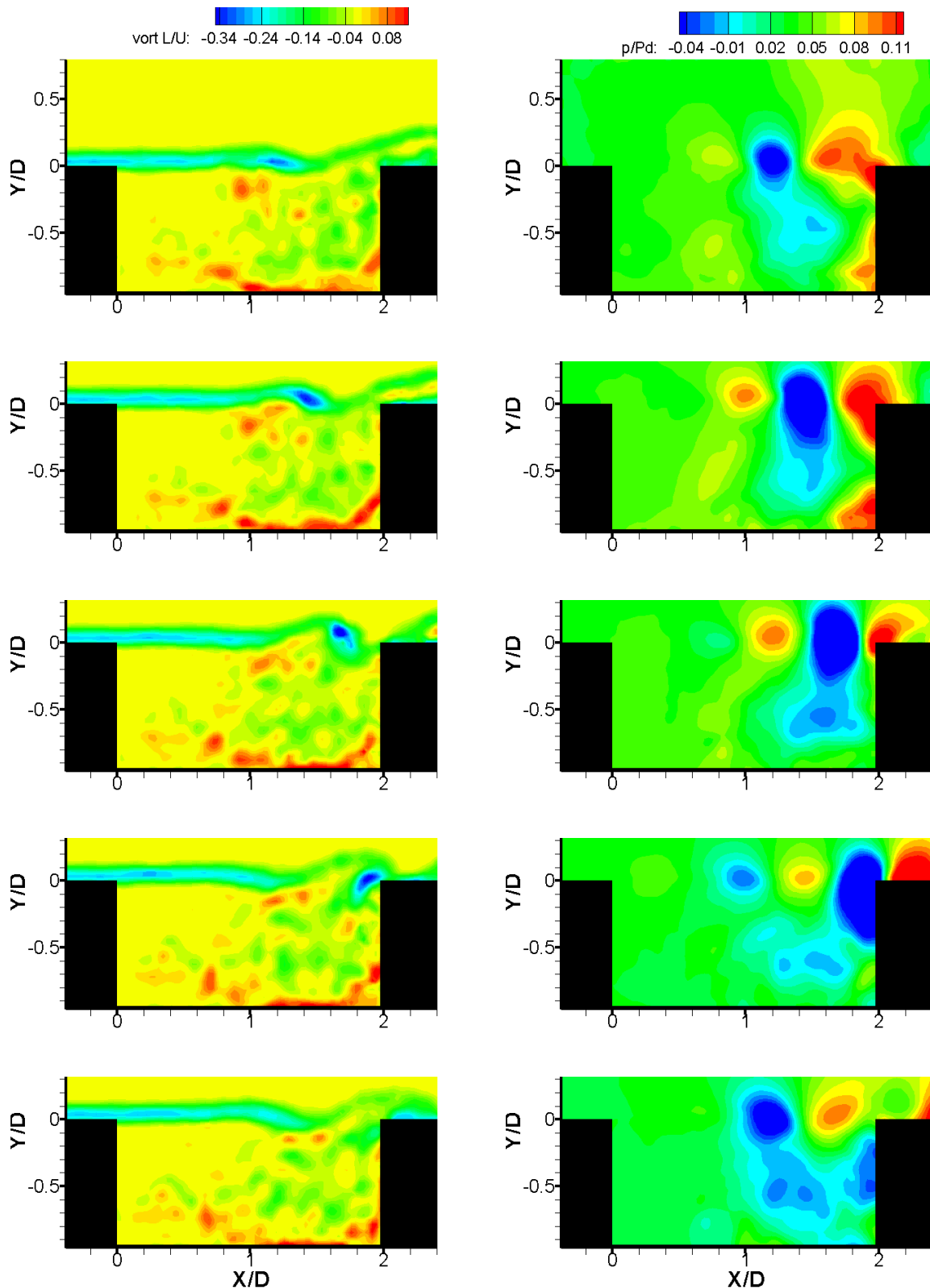


Figure 7.5: Instantaneous Vorticity fields(left) and Pressure fields(right) in a shedding period

7.2 Comparison of PPI results with microphone measurements

Figure (6.2) shows the location of microphones numbered $M1$ to $M11$ placed on the back wall and bottom surface of the cavity. The PIV and microphone measurements were not made simultaneously. To emphasize this in the results presented below, the time history of the sound computed from PIV-PPI are plotted on different time axis marked with (*). Since, the cavity flow has been found to be a stationary process, parameters such as the mean and variance do not change over time.

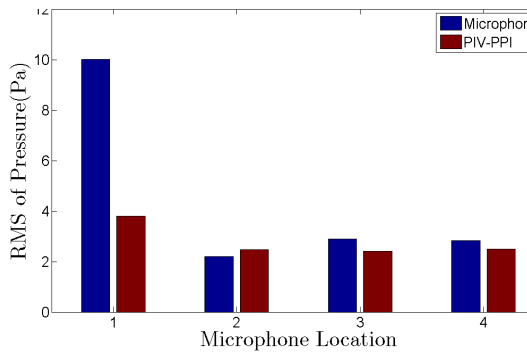
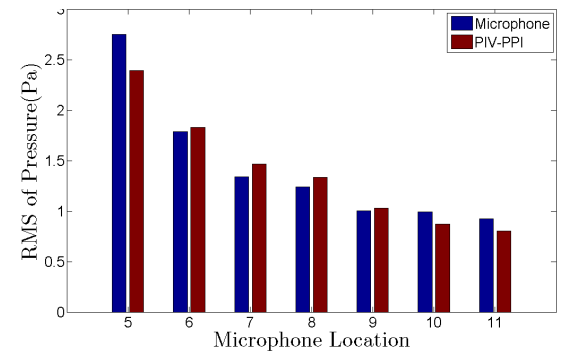
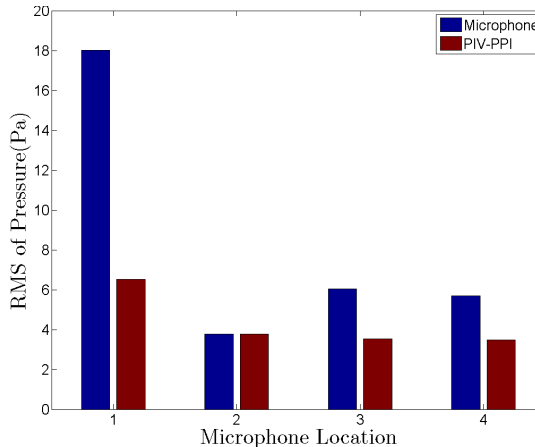
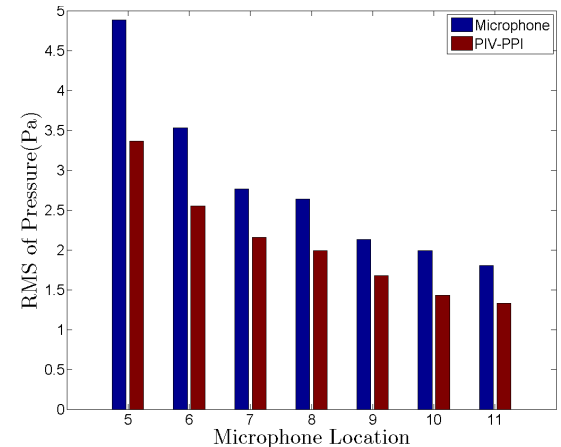
(a) Back wall at $U_e = 10$ m/s(b) Bottom Surface at $U_e = 10$ m/s(c) Back wall $U_e = 12$ m/s(d) Bottom Surface $U_e = 12$ m/s

Figure 7.6: RMS of pressure measured by microphones and pressure computed by PIV-PPI at the same locations for mean flow $U_e = 10, 12$ m/s

A comparison of RMS of pressure measured by microphones and pressure computed by PPI at the same location is presented in the figure (7.6). Spectral analysis of signals are presented as small band spectra of 12 Hz resolution. The values obtained by the two methods show good agreement with an exception at microphone M1. The PPI at this location under-estimates the RMS pressure fluctuations by more than 50%.

The spectral analysis of pressure signal at microphone on the back wall is shown in Figure

(7.7). It can be seen that the PPI technique overestimates the broadband fluctuations but underestimates the tonal peaks with the exception at M1 where both tonal and broadband fluctuations are under-estimated. The discrepancy at microphone, M1 can be attributed to inaccurate mapping of the pathlines for computation of Lagrangian derivatives from PIV data at the leading edge of the cavity. Figure (7.1(c)) shows that in this region the flow is fluctuating with large velocity gradients. The PIV acquisition rate may not be sufficient to resolve these velocity fluctuations and by PPI to follow the pathlines.

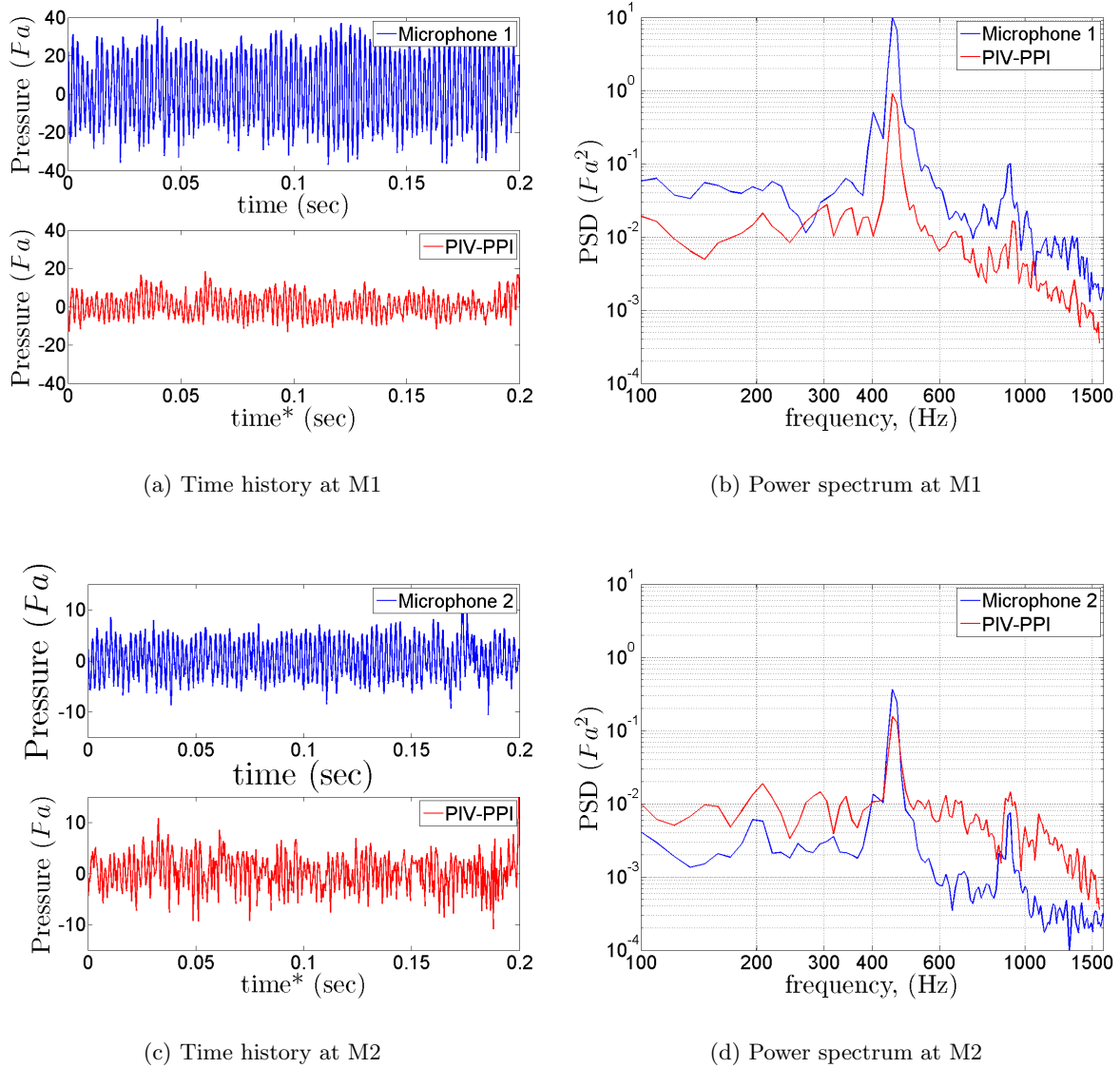


Figure 7.7: Comparison of PPI and microphone back wall at $U_e = 12$ m/s

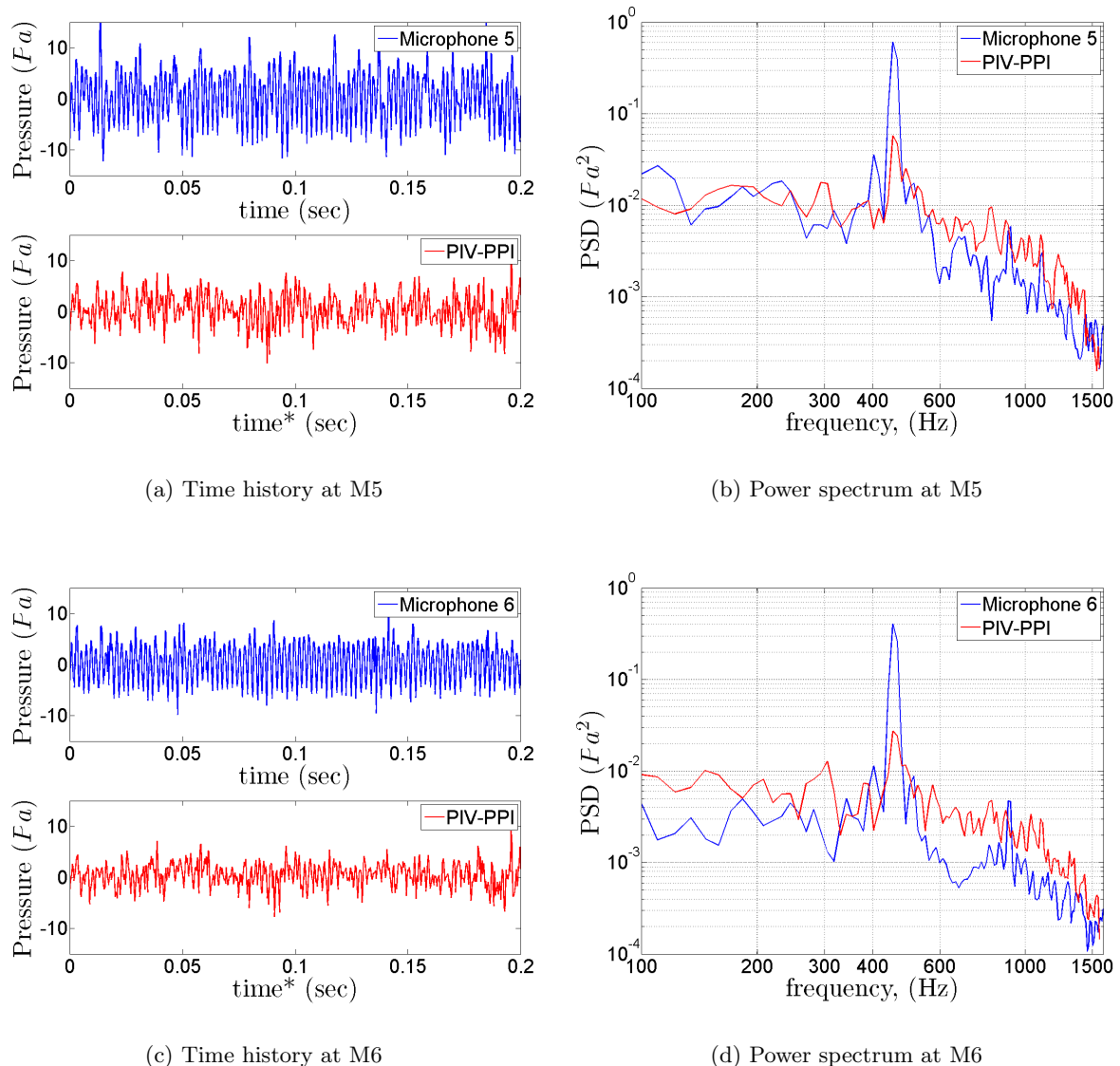


Figure 7.8: Comparison of PPI and microphone on the bottom wall at $U_e = 12 \text{ m/s}$

7.3 Aeroacoustics of cavity flow

The results of the aeroacoustic prediction, obtained by implementation of both Curle's Analogy and Gutin's principle are shown for free stream velocities $U_e = 10, 12$ and 15 m/s. The results are compared with the data from microphones $M13, M14$ in the acoustic-field. The sound pressure level is computed using the definition :

$$SPL = 10 \log_{10} \left(\frac{p_{rms}^2}{p_{ref}^2} \right) \quad (7.1)$$

where, $p_{ref} = 20\mu\text{Pa}$

7.3.1 Comparison of acoustic computations with microphone measurements

The comparison of computed sound and sound measured by microphones (numbered M13 to M15) in acoustic-field is provided. Microphone M12 was found to be broken and hence not included in this report. It may be mentioned again that the PIV and microphone measurements were not made simultaneously. To emphasize this in the results presented below, the time history of the sound computed from PIV-PPI are plotted on different time axis marked with (*). Spectral analysis of signals are presented as small band spectra of 12 Hz resolution.

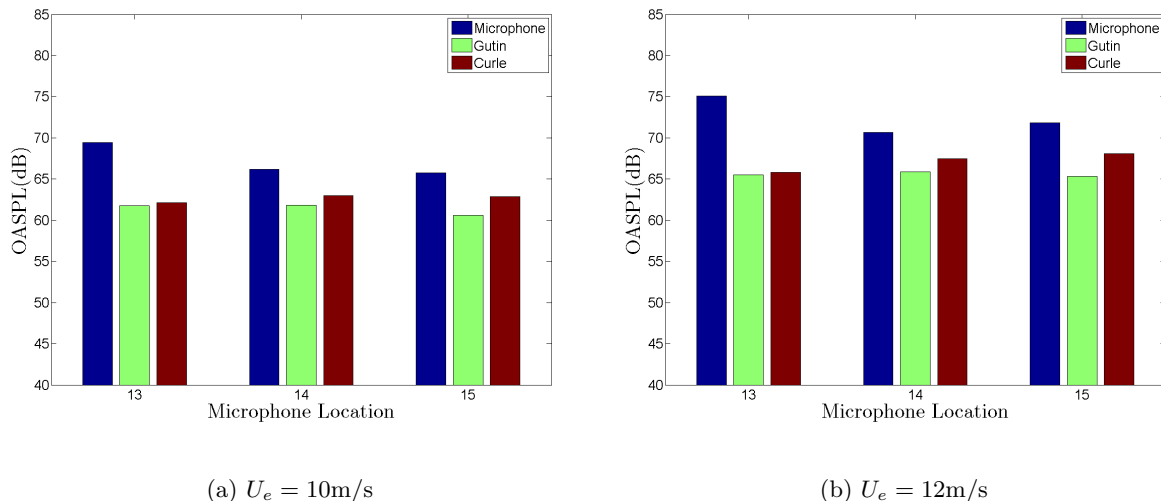


Figure 7.9: Comparison of OASPL of sound measured by microphone in acoustic with Curle's Analogy and Gutin's Principle

Figure(7.9) shows the the (Overall Sound Pressure Level) OASPL of the sound computed by the microphones in the acoustic-field in comparison to the OASPL computed using Curle's analogy and Gutin's principle. It can be observed that Curle's analogy underestimates the sound pressure level by 5 – 10 decibels. Also observe the under prediction of OASPL by Gutin as compared to Curle in the order of 1 – 2 decibels. This can be explained as follows. Gutin's principle (Equation (3.29)) applied in this case is the same as Curles Analogy (Equation

(3.27)) without the contribution from the second integral term. This is consistent with the dimensional analysis of the two surface integral terms (shown in Chapter (3.9.6)) which shows that the second integral must be taken into account to measure the sound in near-field where microphones are located.

The spectral analysis of the sound measured by microphones is presented along with the analysis of sound computed at the same locations from Curle and Gutin in Figure(7.10) for mean stream flow $U_e = 12\text{m/s}$. It can be seen from sub figures (7.10(b), 7.10(d)) both microphone and Curle's Analogy show presence of tonal peaks at the same location. Although the general trend of the acoustic spectra is well captured by Curle's analogy, it is able to estimate neither the broadband or the height of tonal peak accurately.

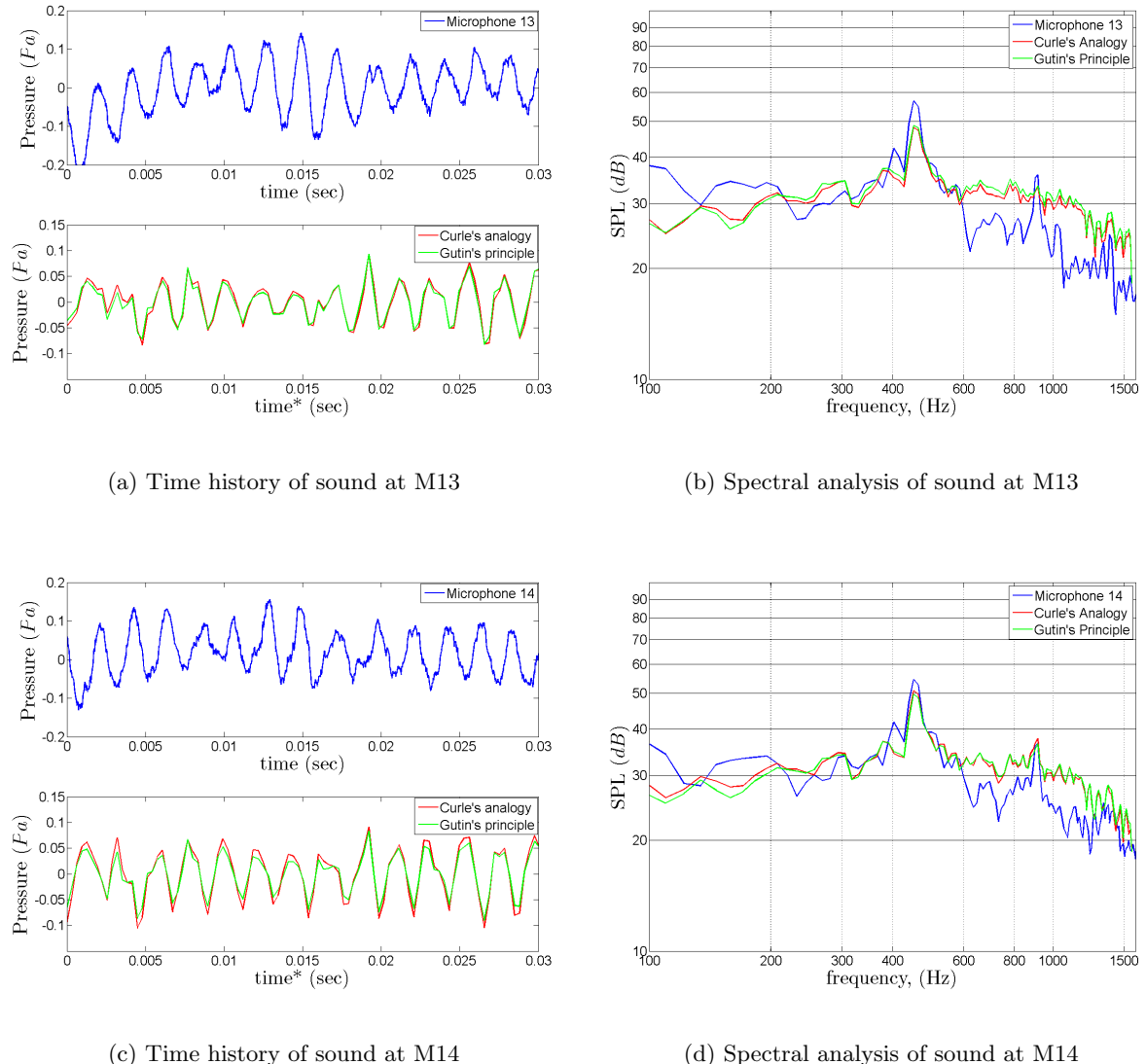
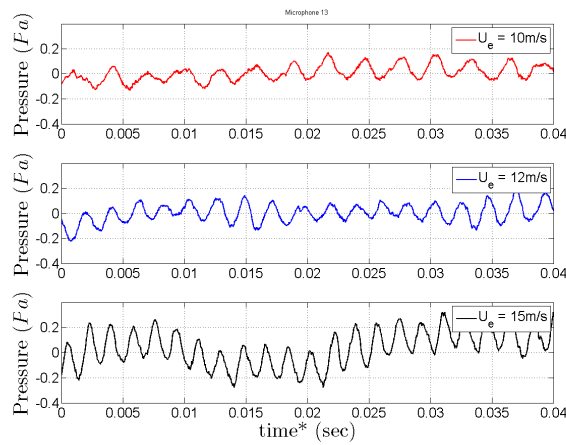


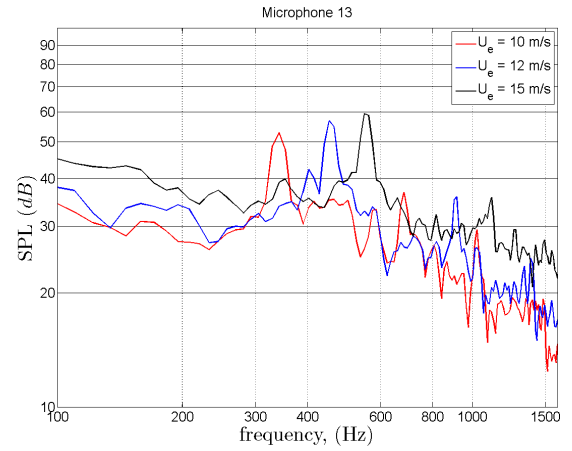
Figure 7.10: Comparison of sound measured by microphones with Curle's Analogy and Gutin's Principle at $U_e = 12 \text{ m/s}$

7.4 Sound generated at different Free Stream Velocities

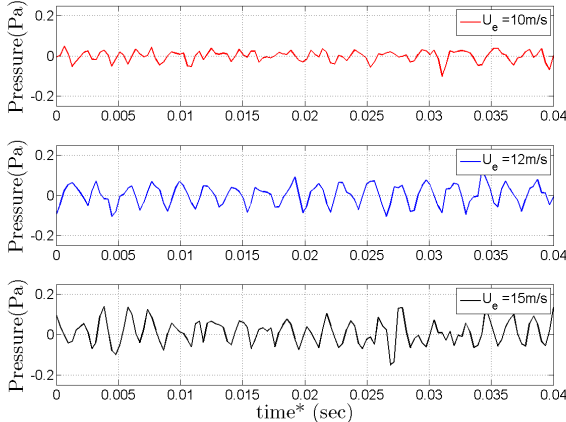
This section presents the variation of sound produced by cavity flow with the free-stream velocity U_e . Figure(7.11(b)) shows the spectra of sound measured by microphone M13. As the speed increases the tonal peaks shift to a higher frequency and show higher decibel level as well. This trend is also captured by the Curle's Analogy shown in Figure (7.11(d)). Figure (7.12) show similar results at microphone M14.



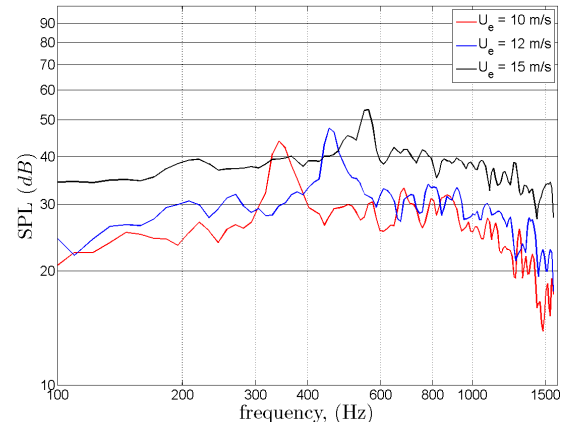
(a) Time history of sound measured by M13



(b) Spectral analysis of sound measured by M13



(c) Time history of sound computed by Curle and Gutin at M13



(d) Spectral analysis of sound computed by Curle and Gutin at M13

Figure 7.11: Variation of sound at M13 with in acoustic-field free stream velocity

The shear layer between an open-jet flow and quiescent air outside the test section refracts the sound generated by the cavity in the flow. Absorption and scattering of sound by shear layer turbulence is also possible. These factors were not taken into account.

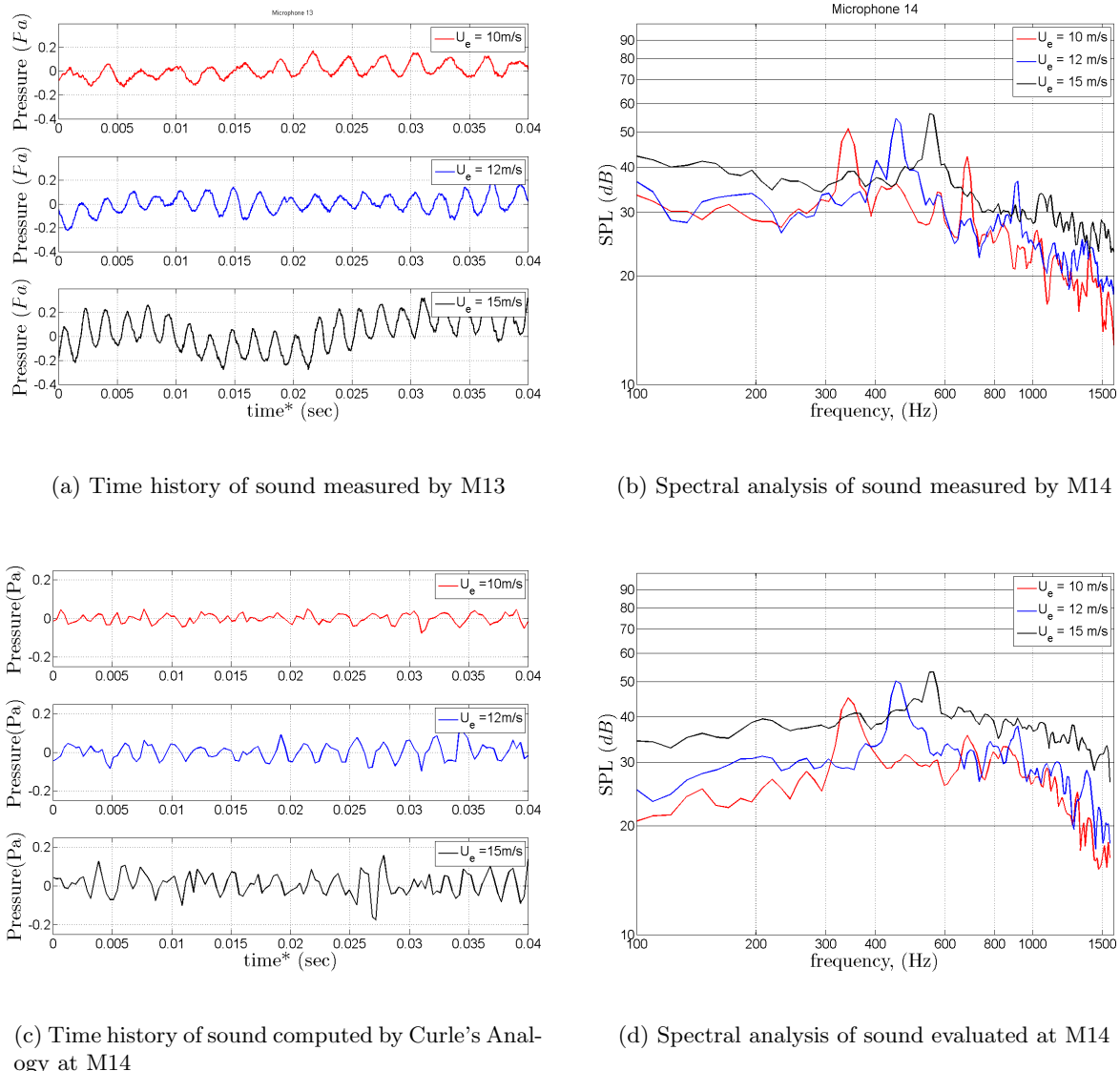


Figure 7.12: Variation of sound with free stream velocity at M14 in acoustic-field

Chapter 8

Conclusion and Recommendation

Aeroacoustic investigation of flow around a rectangular cavity was performed using Two dimensional Temporally Resolved Particle Image Velocimetry(2D-TR-PIV). Velocity fields were obtained from TR-PIV with high temporal and spatial resolution. Pressure fields around the cavity were obtained from the velocity fields by solving Poisson's equation with Lagrangian approach using a Planar Pressure Imaging (PPI) solver. Curle's Acoustic acoustic analogy and Gutin's principle was implemented to evaluate sound generated by the cavity flow from the pressure fields. The pressure fields around the cavity and acoustic predictions were compared to the measurements from microphones placed on the walls of the cavity and in the acoustic-field respectively.

8.1 Conclusions

The dynamics of the cavity flow was analysed and acoustic feedback mechanism was identified to be the dominant mechanism driving the flow. The tonal peaks in the spectra of velocity and pressure occur at the same strouhal number , indicating strong correlation between the vortical motion and pressure fluctuations. The locations of primary tonal peak correspond to Rossiter's second mode indicating that cavity is dominated by acoustic feed-back mechanism. Second harmonic of the tonal peak was also observed.

The goal of this thesis work was to evaluate the feasibility of 2D-TR-PIV for aeroacoustic prediction. It may be concluded that the analysis of aeroacoustic analysis of cavity flow using TR-PIV was able to predict the sound in the acoustic field qualitatively . The locations of the two tonal peaks were well captured as well as the trend of the broad-band noise. However, there was a significant underestimation in quantifying the sound pressure level especially the tonal peaks. The estimation of the secondary peaks was also not satisfactory.

This can be attributed to errors in evaluating the pressure on the walls of the cavity. The walls of the cavity suffer from reflections during PIV image acquisition and cause error in velocity estimation. Although normalization technique provides significant improvement in removing these reflections its effect cannot be completely eliminated. The primary source of sound in cavity has been identified as the back-wall of the cavity which is subject to fluid motion with high turbulence and vortical motion. The planar pressure imaging scheme is unable to follow the path-lines in this region of small speeds, high velocity gradients and fluctuations leading

to errors in pressure estimation. Accurate estimation of pressure fluctuations on the back wall is critical in estimating the sound from the cavity.

The Curle's analogy was compared with Gutin's principle. It is concluded from the dimensional analysis of the equations and implementation that Gutin's principle underestimates the sound pressure level at the microphone locations because it neglects the contribution from the second integral term.

8.2 Recommendation for future work

Three major sources of error in estimation of sound from cavity flow using TR-PIV have been identified by the author:

1. High velocity gradients and fluctuations in the flow
2. Three dimensionality of the flow
3. Reflections from the wall

Tomographic PIV is recommended to quantify the extent of three dimensionality in the flow. This will allow estimation of error in pressure evaluation using planar pressure imaging and develop pressure solvers for three dimensional flow.

To address the problem of large fluctuations in the flow, the acquisition rate must be increased. With continuing breakthroughs in high speed camera and laser technologies, this line of action is feasible. The improvement in spatial resolution of digital cameras will also aid in capturing the smaller scale vortices, which are highly correlated to pressure fluctuations, thus improving pressure evaluation.

The effect of wall reflections can be quantified after the errors due to above factors are isolated and tackled accordingly. PIV interrogation techniques need to be further improved so that the errors in estimating velocities near wall are reduced which crucial in estimating the sound from cavities. Advanced digital signal processing tools must be developed for the analysis of acoustic data.

Bibliography

- S. Abdallah and J. Dreyer. Dirichlet and Neumann boundary conditions for the pressure Poisson equation of incompressible flow. *International Journal for Numerical Methods in Fluids*, 8:1029–1036, September 1988. doi: 10.1002/fld.1650080905. [40]
- K. K. Ahuja and J. Mendoza. Effects of cavity dimensions, boundary layer, and temperature on cavity noise with emphasis on benchmark data to validate computational aeroacoustic codes. *Georgia Tech Research Inst., Atlanta, GA*, 1995. [7, 8]
- T. Baur and J. Kongeter. Piv with high temporal resolution for the determination of local pressure reductions from coherent turbulence phenomena. In *3rd International Workshop on Particle Image Velocimetry*, 1999. [41]
- P. J. W. Block. Noise response of cavities of varying dimensions at subsonic speeds. Technical report, December 1976. [7]
- T. Colonius and S. K. Lele. Computational aeroacoustics: progress on nonlinear problems of sound generation. *Progress in Aerospace Sciences*, 40:345–416, August 2004. doi: 10.1016/j.paerosci.2004.09.001. [13, 69, 71]
- N. Curle. The influence of solid boundaries upon aerodynamic sound. *Proceedings of the Royal Society of London. Series A, Mathematical and Physical Sciences*, 231(1187):505–514, 1955. ISSN 00804630. [3, 14, 16]
- J. E. Ffowcs Williams. Hydrodynamic Noise. *Annual Review of Fluid Mechanics*, 1:197–222, 1969. [14]
- M. Gharib and A. Roshko. The effect of flow oscillations on cavity drag. *Journal of Fluid Mechanics Digital Archive*, 177(-1):501–530, 1987. doi: 10.1017/S002211208700106X. [9]
- P. M. Gresho and R. L. Sani. On pressure boundary conditions for the incompressible Navier-Stokes equations. *International Journal for Numerical Methods in Fluids*, 7:1111–1145, October 1987. doi: 10.1002/fld.1650071008. [40]
- R. Gurka, A. Liberzon, D. Hefetz, D. Rubinstein, and U. Shavit. Computation of pressure distribution using PIV velocity data. In *In Proc. of the 3rd 3rd International Workshop on Particle Image Velocimetry*, Santa Barbara, CA, Sep 1999. [41]

- C. Haigermoser. Application of an acoustic analogy to PIV data from rectangular cavity flows. *Experiments in Fluids*, pages 40–+, March 2009. doi: 10.1007/s00348-009-0642-5. [22, 40]
- H. H. Heller, D. G. Holmes, and E. E. Covert. Flow-induced pressure oscillations in shallow cavities. *Journal of Sound Vibration*, 18:545–545, October 1971. doi: 10.1016/0022-460X(71)90105-2. [7]
- K. Krishnamurty. Acoustic radiation from two-dimensional rectangular cutouts in aerodynamic surfaces. *NASA Technical Reports*, NACA-TN(3487):34, 1955. doi: 19930084329. [10]
- J. Larsson, L. Davidson, L.-E. Eriksson, and M. Olsson. Aeroacoustic Investigation of an Open Cavity at Low Mach Number. *AIAA Journal*, 42:2462–2473, December 2004. doi: 10.2514/1.1339. [17, 18]
- M. J. Lighthill. On sound generated aerodynamically. i. general theory. *Proceedings of the Royal Society of London. Series A, Mathematical and Physical Sciences*, 211(1107):564–587, 1952. ISSN 00804630. [3, 14, 17]
- Xiaofeng Liu and Joseph Katz. Instantaneous pressure and material acceleration measurements using a four-exposure piv system. *Experiments in Fluids*, 41(2):227–240, Aug 2006. [40, 42]
- D. J. Maull and L. F. East. Three-dimensional flow in cavities. *Journal of Fluid Mechanics Digital Archive*, 16(04):620–632, 1963. doi: 10.1017/S0022112063001014. [8]
- S. Tanahashi N. Fujisawa and K. Srinivas. Evaluation of pressure field and fluid forces on a circular cylinder with and without rotational oscillation using velocity data from piv measurement. *Measurement Science and Technology*, 2005. [41]
- D. Rockwell and E. Naudascher. Review - Self-sustaining oscillations of flow past cavities. *ASME Transactions Journal of Fluids Engineering*, 100:152–165, June 1978. [5]
- Roeland de Kat, Bas W. van Oudheusden, and Fulvio Scarano. Instantaneous planar pressure field determination around a square-section cylinder based on time-resolved stereo-piv. In *14th Int Symp on Applications of Laser Techniques to Fluid Mechanics*. [41, 42, 43]
- J. E. Rossiter. Wind-tunnel experiments on the flow over rectangular cavities at subsonic and transonic speeds. *Journal of Fluid Mechanics Digital Archive*, (3438), 1964. [5, 7, 8]
- V. Sarohia, editor. *Experimental investigation of oscillations in flows over shallow cavities*, January 1976. [8, 9]
- F. Scarano and M. L. Riethmuller. Iterative multigrid approach in PIV image processing with discrete window offset. *Experiments in Fluids*, 26:513–523, 1999. [36]
- K. Takeda and C. M. Shieh. Cavity tones by computational aeroacoustics. *International Journal of Computational Fluid Dynamics*, 18(6), 2004. [8, 69]
- C. K. W. Tam. The acoustic modes of a two-dimensional rectangular cavity. *Journal of Sound Vibration*, 49:353–364, December 1976. doi: 10.1016/0022-460X(76)90426-0. [7]

M. Wang, J. B. Freund, and S. K. Lele. Computational Prediction of Flow-Generated Sound. *Annual Review of Fluid Mechanics*, 38:483–512, January 2006. doi: 10.1146/annurev.fluid.38.050304.092036. [71]

Appendix A

Computational Aeroacoustics (CAA)

The use of computational fluid dynamics and, more recently, computational aeroacoustics to simulate the flow over open cavities has enabled researchers to gain deeper insights into flow physics and acoustics, and provides a means of estimating not only the frequency but also amplitude of the dominant tones.

A wide range of flow simulation methodologies can be used to study the problems of sound generation [Colonius and Lele \(2004\)](#) have given a review on current research on non-linear problems of sound generation, with special discussion on hierarchy of computational methodologies and their numerical aspects . [Takeda and Shieh \(2004\)](#) highlight the state-of-the- art computational aeroacoustic (CAA) simulations on unsteady cavity flow. These methodologies can be grouped according to the range of spatial and temporal scales that are explicitly represented in the simulation. The influence of the flow details that are not captured requires modeling. But apart from this, any specific approach may or may not aim to represent the sound that is generated by the unsteady flow. Accordingly the methods fall under two broad categories:

1. Direct approaches (DNS, LES, VLES, DES)
2. Hybrid approaches (DNS+LEE, LES+BEM, RANS+SNGR, etc.)

A.1 Direct Approaches

The direct approach aims to compute the sound together with its fluid dynamic source field by solving the compressible flow equations. The simulation domain must be sufficiently large to include all the sound sources of interest and at least part of the acoustic near field. Extension to the acoustic far field can then be achieved using a variety of analytical and numerical means.

A **Direct Numerical Simulation (DNS)** is a simulation in computational fluid dynamics in which the Navier-Stokes equations are numerically solved without any turbulence model. This means that the whole range of spatial and temporal scales of the turbulence must be resolved. All the spatial scales of the turbulence must be resolved in the computational mesh, from the smallest dissipative scales (Kolmogorov microscales), up to the integral scale

L , associated with the motions containing most of the kinetic energy. The memory storage requirement in a DNS grows very fast with the Reynolds number

$$N_{3D} = Re^{9/4} \quad (\text{A.1})$$

where, N_{3D} = number of mesh points required to resolve all the spatial scales,
 Re = Reynolds number of the flow,

To perform a DNS on a cavity flow of $Re_L = U_\infty L/\nu = 3000$, the number of mesh points($(N_{3D})^{9/4}$) exceeds $60E6$. Thus, DNS requires tremendous amount of memory storage and computational time which is both expensive and unfeasible for industrial or research purpose. Its use is limited to simple flow configurations at low to moderate Reynolds numbers. The direct computation method using DNS, because it avoids any modeling approximations, provides a tool for studying sound-generation mechanisms and generating databases for developing and evaluating other sound prediction models.

The Reynolds-averaged NavierStokes (RANS) equations are equations of motion for fluid flow averaged over a period that is short compared to the flow time evolution, but large compared to the time-scale of the turbulent fluctuations. The effect of turbulent fluctuations is accounted for by so called turbulence model. The most used models are Reynold's stress model: $(k - \epsilon, k - \omega)$. Compressible unsteady RANS simulations are used widely to compute both subsonic and supersonic cavity flows, but with varying degrees of success. The use of first- and second-order CFD solvers requires fine grids and time steps in order to resolve acoustic waves due to their generally poor dissipation and dispersion properties.

Large Eddy Simulations Barring any dramatic improvements in RANS-based noise models, LES offers the best promise in the foreseeable future for noise prediction at Reynolds numbers of practical interest. It copes with the well-known Reynolds number limitation of DNS by only explicitly representing the large turbulence scales in the flow, and models the effect of the smaller scales. The mathematical formalism for LES is established through a spatial filtering operation applied to the Navier-Stokes equations, which results in unclosed subgrid-scale (SGS) stress terms. Because the small-scale motions are more universal than the large-scale motions, SGS modeling is expected to be more robust than turbulence modeling in the RANS context.

A.2 Hybrid Approaches

In a hybrid approach, the computation of flow is decoupled from the computation of sound, which can be done in a post-processing step based on an aero-acoustic theory or a flow-field decomposition. In some cases this can be carried out concurrently with the flow simulation.

A hybrid approach is also attractive when only part of the sound can be computed directly. For example, in LES the smaller flow scales may be either absent or inaccurate. The sound of these missing scales can be added to the direct solution using acoustic theory.

A possible approach to extend the near field compressible flow data to the radiated acoustical field is the numerical solution of **Linearized Euler equations (LEE)** with source-terms. The numerical difficulty of this approach stem from the fact that the LEE admits non-trivial instability wave solutions of the homogeneous equations (i.e. with zero source terms). As

these instability waves grow, they contaminate the near acoustic field and the errors inherent in the boundary schemes or mesh non-uniformities spuriously reflect them into radiating acoustic waves.

A feasible solution to overcome instability problems is the use of **Acoustic Perturbation Equations** wherein an additional irrotational assumption is made for the acoustic velocity field (Crocco's theorem).

In recent years several groups have proposed new methods of Hybrid CAA like **Incompressible/acoustic split, hybrid RANS/LES or DES** methods. An extensive review of these emerging methods can be found in , [Colonius and Lele \(2004\)](#) and [Wang et al. \(2006\)](#).

1. The generation of acoustic waves by fluid motion is, by its nature, an unsteady process; steady flows generate no sound. Turbulence modeling, leading to RANS, unsteady RANS, and LES, filters small spatial and high frequency fluctuations from the solution; the impact of such filtering on sound generation has not yet been characterized in any systematic way. Modern turbulence simulation techniques such as DNS, LES, or integrated RANS/LES methods offer attractive alternatives, but they are not always affordable even with todays high-performance computers. The latter two of these approaches involve different levels of modeling and approximation whose effects on noise prediction have not been thoroughly examined.
2. Acoustic waves may propagate coherently, with very low attenuation due to viscous effects, over long distances in the flow. Artificial dissipation and dispersion at a level that may be tolerable for hydrodynamic fluctuations can lead to unacceptable attenuation of acoustic waves.
3. even loud flows radiate a very small fraction of their total energy as sound. That is, acoustic (radiation) efficiency is invariably very low. At low Mach number, acoustic inefficiency can be viewed as the result of a delicate cancellation process of equal but nearly opposite sources (e.g. dipole, quadrupole, etc.). Numerical errors that may upset this delicate balance can therefore lead to serious overestimates of sound generation. For example, truncation of a computational domain with artificial boundary conditions is a primary cause of such errors.

Appendix B

Sonoion 8000 Microphones

Soinion 8000 series microphones are condenser microphones. They are electric transducers which use a capacitor to convert acoustical energy into electrical energy. Condenser microphones require power from a battery or external source. The resulting audio signal is stronger signal than that from a dynamic. Condensers also tend to be more sensitive and responsive than dynamics, making them well-suited to capturing subtle nuances in a sound. They have an omni symmetrical response.

Working principle

A capacitor has two plates with a voltage between them. In the condenser mic, one of these plates is made of very light material and acts as the diaphragm. The diaphragm vibrates when struck by sound waves, changing the distance between the two plates and therefore changing the capacitance. Specifically, when the plates are closer together, capacitance increases and a charge current occurs. When the plates are further apart, capacitance decreases and a discharge current occurs.

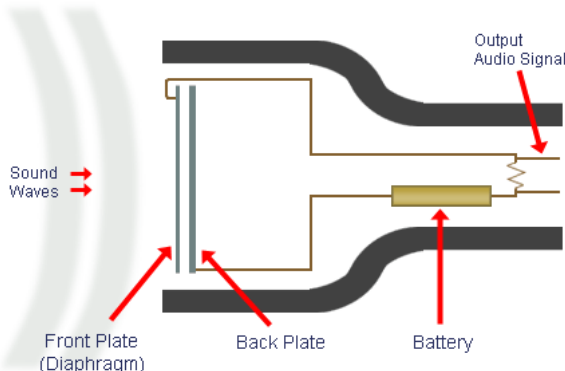


Figure B.1: Schematic description of condenser microphones

Typical Frequency Response

Frequency response refers to the way a microphone responds to different frequencies. Each microphone has a characteristic frequency-response curve. The figure below is the frequency response curve of Sonoion 8000 series microphones.

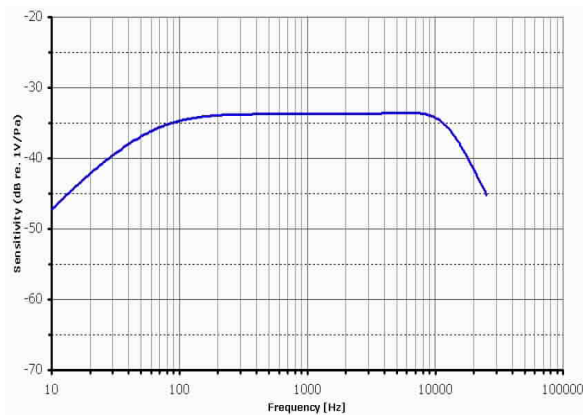


Figure B.2: Typical response curve for Sonoion 8000 series microphones